END
DATE
FILMED.
1 -81
DTIC

$4\ NRL\ MR\ 4369$

⑨ REPORT DOCUMENTATION PAGE		READ INSTRUCTIONS BEFORE COMPLETING FORM
1. REPORT NUMBER NRL Memorandum Report 4369	2. GOVT ACCESSION NO. AD-1092470	3. RECIPIENT'S CATALOG NUMBER
4. TITLE (and Subtitle) NRL INERTIAL CONFINEMENT FUSION THEORY PROGRAM 1979 ANNUAL REPORT, OCTOBER 1978 – DECEMBER 1979		5. TYPE OF REPORT & PERIOD COVERED Interim report on a continuing NRL problem
7. AUTHOR(s) The Laboratory for Computational Physics and The Plasma Physics Division		6. PERFORMING ORG. REPORT NUMBER
		8. CONTRACT OR GRANT NUMBER(s) NRL Problem 62-0575-0-0
9. PERFORMING ORGANIZATION NAME AND ADDRESS Naval Research Laboratory Washington, D.C. 20375		10. PROGRAM ELEMENT, PROJECT, TASK AREA & WORK UNIT NUMBERS
11. CONTROLLING OFFICE NAME AND ADDRESS Department of Energy Office of Laser Fusion Washington, D.C. 20545		12. REPORT DATE 20 Nov 1980 13. NUMBER OF PAGES 74
14. MONITORING AGENCY NAME & ADDRESS(if different from Controlling Office)		15. SECURITY CLASS. (of this report) UNCLASSIFIED
		15a. DECLASSIFICATION/DOWNGRADING SCHEDULE

16. DISTRIBUTION STATEMENT (of this Report)

Approved for public release; distribution unlimited.

17. DISTRIBUTION STATEMENT (of the abstract entered in Block 20, if different from Report)

18. SUPPLEMENTARY NOTES

This work was sponsored by the Department of Energy, Project No. NP-01-05-01; NP-02-01

19. KEY WORDS (Continue on reverse side if necessary and identify by block number)

Inertial Confinement Fusion Computational Fluid Dynamics
Laser Light Absorption Rayleigh-Taylor Instability
Ablative Acceleration
Light Ion Beams

20. ABSTRACT (Continue on reverse side if necessary and identify by block number)

This is the 1979 annual report of the NRL Inertial Confinement Fusion Theory Program. It covers research performed from October 1978 through December 1979. Research in each of the four current program areas is reported:
Section A. Laser Light Absorption.
Section B. Fluid Dynamics of Ablative Acceleration.
Section C. Development of Computational Techniques.
Section D. Rayleigh-Taylor Stabilization Techniques.
(Continued)

DD FORM 1473 EDITION OF 1 NOV 65 IS OBSOLETE
1 JAN 73
S/N 0102-014-6601

i

20. ABSTRACT (Continued)

Our work in Section A includes an analysis of anomalous absorption, backscatter and flux limitation in laser-produced plasmas. The physical processes included in the model are inverse bremsstrahlung, resonant absorption, absorption by ion-acoustic fluctuations, and Brillouin backscatter. In Section B we report our work on the energy conversion of light ion beams through the ablative acceleration of thin foils, our work on spherical shock implosion dynamics and stability, and our 1D and 2D work on the dynamics of laser-driven thin plastic foils. In Section C we report our current developments in triangular grid techniques. These results include improved calculations of the Rayleigh-Taylor instability through higher resolution in the SPLISH numerical model. In Section D, we report our improved understanding of the "quasi-static" equilibria. We also report on our development of a vorticity generation model to study the Rayleigh-Taylor instability and include our results for test problem and actual laser-driven ablation layer profiles. We also include our work on the Rayleigh-Taylor eigenvalue problem.

The report concludes with a small section on our plans for the extension and continuation of this research. Footnotes, figures, and references for each section below are compiled separately.

CONTENTS

NRL INERTIAL CONFINEMENT FUSION THEORY PROGRAM
1979 ANNUAL REPORT
OCTOBER 1978—DECEMBER 1979

INTRODUCTION

This is the 1979 annual report of the NRL Inertial Confinement Fusion Theory Program. It covers research performed from October 1978 through December 1979. Research in each of the four current program areas is reported:

Section A. Laser Light Absorption.

Section B. Fluid Dynamics of Ablative Acceleration

Section C. Development of Computational Techniques.

Section D. Rayleigh-Taylor Stabilization Techniques.

Our work in Section A includes an analysis of anomalous absorption, backscatter, and flux limitation in laser-produced plasmas. The physical processes included in the model are inverse bremsstrahlung, resonant absorption, absorption by ion-acoustic fluctuations, and Brillouin backscatter. In Section B we report our work on the energy conversion of light ion beams through the ablative acceleration of thin foils, our work on spherical shock implosion dynamics and stability, and our 1D and 2D work on the dynamics of laser-driven thin plastic foils. In Section C we report our current developments in triangular grid techniques. These results include improved calculations of the Rayleigh-Taylor instability through higher resolution in the SPLISH numerical model. In Section D, we report our improved understanding of the "quasi-static" equilibrium for laser-driven ablation layers, and discuss the evolutionary trends for the various possible "quasi-static" equilibria. We also report on our development of a

vorticity generation model to study the Rayleigh-Taylor instability and include our results for test problem and actual laser-driven ablation layer profiles. We also include our work on the Rayleigh-Taylor eigenvalue problem.

The report concludes with a small section on our plans for the extension and continuation of this research. Footnotes, figures, and references for each section below are compiled separately.

A. LASER LIGHT ABSORPTION

The absorption and backscatter of light in the underdense blowoff of a laser produced plasma, as well as limitiation on electron thermal energy flux all play important roles in laser fusion. This year's work has been a continuation of our earlier work in this area[1,2] and models the dynamics of the interaction rather than the steady state. Also included in this effort has been a study of the effects of Brillouin backscatter. Although our work applies in principle to any laser produced plasma, it is particularly motivated by experiments at the Naval Research Laboratory on planar targets.[3-6] Experiments here have demonstrated that backscatter through the lens (apparently Brillouin backscatter) can be a very important process for structured laser pulses at sufficiently high intensity.[3-4] Also, more recent experiments with longer pulses[5] (pulse duration of about 3 nsec) have shown very high absorption even at intensities where inverse bremsstrahlung is not effective. For instance at an irradiance of 7×10^{14} W/cm^2, the fractional absorption is about 60%. Experiments at NRL[6] and elsewhere[7] also have shown that absorption is enhanced when the target is in the focal plane of the lens. It has always been our opinion that resonant absorption alone cannot account for all of the absorption.[2] Reference 2 reviews absorption measurements done at many laboratories and comes to this conclusion. The additional mechanism which we propose is ion acoustic turbulence driven by the return current. That mechanism takes place in either an unmagnetized[1] or magnetized[2] plasma. The fluid simulations reported here attempt to model this process. A very much oversimplified picture is that ion acoustic turbulence in the underdense plasma begins to take over where classical inverse bremsstrahlung becomes ineffective. For instance, the solid line in Figure A.1 is a schematic of the total electron-ion momentum exchange collision frequency as a function of laser irradiance for a Nd laser produced plasma. The dotted line is a

plot of the classical inverse bremsstrahlung, while the dashed line is a plot of the effect of the ion acoustic instability. Roughly speaking, ion acoustic turbulence at high temperature gives perhaps half as much absorption as inverse bremsstrahlung at low temperature.

One of the principal conclusion of this work is that the absorption physics falls into two different regimes. In short single pulse experiments, resonant absorption is the dominant process, but it gets a strong boost from the ion acoustic turbulence. Typically the total absorption is about 40% with resonant absorption accounting for 25% and ion acoustic turbulence for 15%. Most of the light is specularly reflected, although stimulated Brillouin backscatter plays a role also. On the other hand, for long pulses or structured pulses, the physics seems to be dominated by a relatively complicated interplay between backscatter and ion acoustic turbulence. Both of these processes depend upon the quasi-linear and nonlinear behavior of a plasma instability, so the physics is necessarily more speculative than, for instance, absorption by inverse bremsstrahlung. This modeling is more complicated in a fluid simulation but can nevertheless bring a more complete picture of absorption in laser-plasma interactions. Our treatment of these processes is internally self-consistent and is based upon well documented theories, simulations and experiments.

We will now briefly contrast our approach to the physics of the underdense plasma with particle simulations and other fluid simulations. Particle simulations have been particularly useful in studying resonant absorption[8-10], strongly driven backscatter instabilities in a laser produced plasma[11] and current driven ion acoustic instabilities in infinite homogeneous plasmas. The problem with the latter two processes is that they are slow compared to the laser frequency so that particle simulations get very expensive. For instance, the simulation of Brillouin backscatter in Ref. 11 ran to $t = 7 \times 10^3/\Omega$ (35,000 time steps) with $V_{os}/V_e \sim 7$. However, this is only 3.5 psec for a Nd laser produced plasma, and the total length corresponds to only 10 μm, meaning a density gradient scale length of 1-2 μm. Clearly, a particle simulation for more realistic times, lengths and smaller V_{os}/V_e fields would be astronomically expensive. Our approach sacrifices the detailed description of the instabilities. Its effect is now modeled by anomalous transport in a fluid code. However we gain tremendously in the range of

parameters that can be studied. For instance, for a 70 psec Nd laser pulse, we model the entire under-dense plasma for the entire pulse duration with less than two minutes computing time with a TI-ASC.

The other approach, used to study laser-plasma interactions, is fluid simulations (characterized by LASNEX[12-15]). Our simulations have more in common with them than they do with particule simulations but there are still important differences. Specifically our treatment of flux limitation is quite different. In our model, a large thermal flux excites an instability. This instability tends to limit the flux, and gives rise to several other anomalous transport effects. All of these transport effects can be self-consistently related to each other through the turbulence level. To estimate this level we appeal to previous experiment, simulation and theory. Thus flux limits are derived in this work, not specified. Also this work incorporates a model for Brillouin backscatter and, as discussed in the next section, our approach to electron thermal energy transport is quite different from that used in LASNEX.[15]

In the next section we discuss the anomalous physical processes in our simulation models. Detailed results for this work including simulations and comparisons with experiment may be found in NRL Memorandum Report 4083.
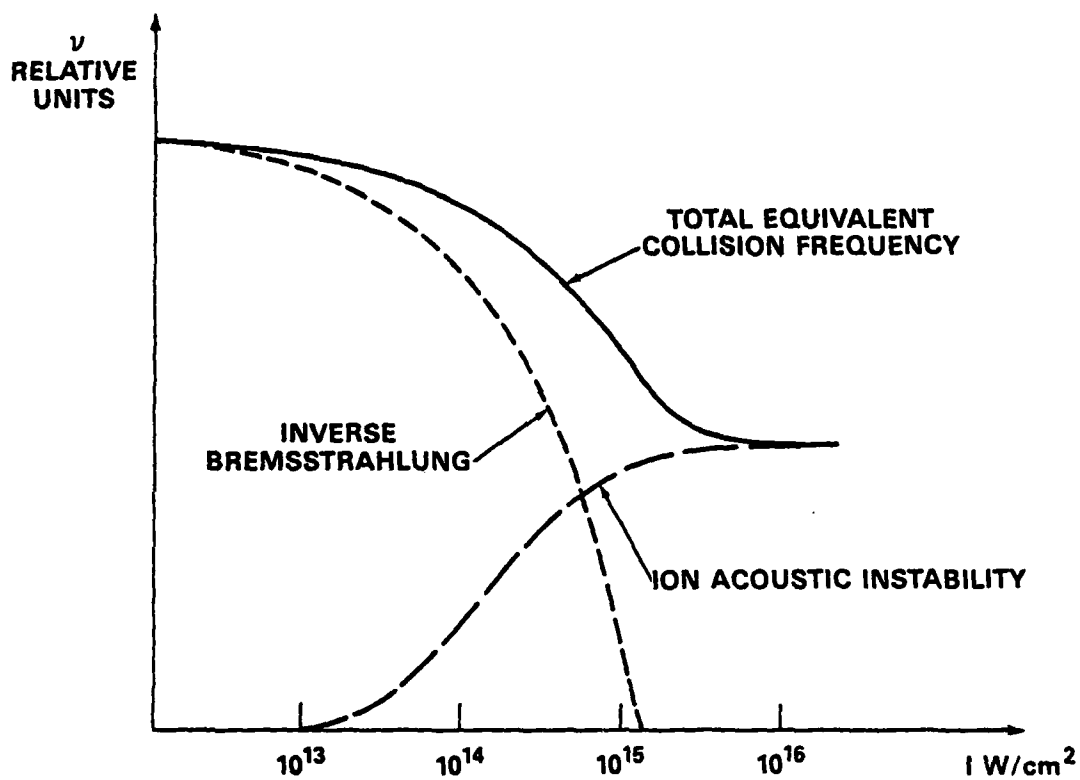
Fig. A.1 — Schematic diagram of importance of inverse bremsstrahlung and ion acoustic turbulence as a function of irradiance (for *Nd* laser light)

A1. Anomalous Physical Processes

A1a. Ion Acoustic Instability Generated by Return Current

The problem of the ion acoustic instability in a plasma which conducts energy has been discussed in a series of papers which deal with both unmagnetized[1,16] and magnetized[2,17] plasmas. In our present work we confine our study to unmagnetized plasmas. The basic idea is that if the electrons conduct energy but carry no net current, the flux of energetic particles in the direction of Q (the heat flux) must be balanced by a return current of low velocity particles in the opposite direction. This return current can excite ion acoustic waves which also propagate opposite to Q. There are four principal physical effects of this instability. First of all it reduces the energy flux, or in other words, reduces the electron thermal conduction. Second, it gives rise to an anomalous energy exchange between electrons and ions, with the ions gaining energy and the electrons losing. Third, it gives rises to an electric field which generates the return current (this latter process is not directly calculated in our work because we deal only with the total momentum, not with the momentum of each species separately). These three processes are discussed in detail in Ref. 16.

Fourthly, the ion density fluctuations give rise to enhanced absorption of the laser light.[1,2,16,18] Since our results depend upon $e\phi/T_e$ and the cone angle of the turbulent spectrum θ, it is important to pick these parameters as accurately as possible. Fortunately we can draw on a great deal of experimental data[19-26] and particle simulations[27-33] on current driven ion acoustic instabilities. There is also a great deal of recent theory[34-38] which examines ion trapping, resonance broadening or anomalous transport and which supports these data. Our basic assumption is that an ion acoustic instability driven by a return current will have the same fluctuation level and angular spread as one driven by a real current. Also we model the spectrum with a single k. A choice $\theta \approx \pi/3$, $k \sim k_D/2$ and $\dfrac{e\phi}{T_e} = 0.1$ seems to be reasonably consistent with the data which we have cited.

Let us finally note that if the plasma is magnetized, the ion wave has its wave vector perpendicular to both $\underline{B}$ and $\underline{\nabla} T_e$, so the wave vector can be parallel to the electric field over part of the laser spot.

Thus not only can the absorption be enhanced, but also there is no need to make any assumption concerning angular width of the specturum. Our study, which neglects $\underline{B}$, then gives rise to minimum anomalous absorption.

A1b. Brillouin Backscatter

We now discuss the Brillouin backscatter instability in an inhomogeneous plasma.[39,40,41] Since the flow velocity in the underdense plasma is generally supersonic, we assume that the group velocity of the reflected wave and acoustic wave are in the same (outward) direction. However, even if the group velocities have opposite sign, the result of the theory is not different.[39,42]

For the case without Landau damping of the sound wave, the reflected wave travels back towards the laser, and is spatially amplified for distances less than a length L_c based on the the growth rate of the Brillouin backscatter instability. But if the sound wave is strongly damped then the critical length is based on the Landau damping rate for the wave.

If this linear theory is used, the result is that Brillouin backscatter is an extraordinarily strong process and it dominates the dynamics (that is, the laser light is almost totally reflected) for nearly all gradient scale lengths and incident laser light intensities. Particle simulations have also confirmed that while in the linear regime, Brillouin backscatter can play a dominant role even if the gradient scale length is of order of a free space wavelength.[11] Thus a crucial problem is to see whether any process reduces the strength of Brillouin backscatter instability.

We consider a nonlinear reduction in the growth rate due to ion trapping by the ion acoustic wave. To start, we will show that as the ion wave grows, it is forced into a nonlinear regime. For temporal growth, without Landau damping, each photon of incident wave lost produces one photon of reflected light and one phonon of ion acoustic wave. For spatial growth, the situation is different because the group velocity of the photon is much greater than the group velocity of ion acoustic wave.[42,44]

Now let us consider ion trapping. An ion will trap if the peak-to-peak potential energy drop of the acoustic wave is greater than the difference in energy between the wave phase velocity and $\sqrt{3}$ times

7

the ion thermal energy (assuming a waterbag distribution function for the ions[37]). Also, for trapping to have a significant effect on the ion distribution function, the trapping width must be larger than the ion thermal speed. Thus we have a double condition for ion trapping. For any reasonable parameters, the saturation amplitude of the fluctuating potential of the ion acoustic wave is much larger than that required for ion trapping. Therefore, before the photon can be strongly backscattered, the ion acoustic wave is driven into a strongly nonlinear regime.

To describe the backscatter in this regime, we invoke recent theoretical work.[37,45] Our work does not utilize an enhanced damping, but rather a modification to the growth rate in the absence of damping. The idea is that there is some power input to the ion acoustic wave. In the linear regime, this power input causes the ion acoustic wave to grow at the proper linear growth rate. However once the ions begin to trap, a small increase in amplitude of the ion acoustic wave traps a few more ions. Since ions abruptly gain a tremendous amount of energy when they are trapped, the power input goes principally into accelerating ions and only slightly into causing wave growth. However the wave does not stop growing completely because the power input is still there. Nevertheless, the growth rate does abruptly drop once ions begin to trap. The calculation of the growth rate is given in Ref. 37 for a wave which grows in time in an homogeneous plasma and in Ref. 45 for a wave which grows in space in an homogeneous but bounded plasma.

In summary, our non-linear treatment of stimulated Brillouin backscatter which includes pump depletion, ion heating relies on reducing the linear growth rate γ_o and the coherent scattering length L_c. It is significantly different from other SBS treatments[51] which rely mostly on increasing L_c until it is longer than the plasma size.

A1c. The Problem of Energetic Electrons

Other numerical studies of this problem, principally LASNEX have assumed that the electron energy is transported mostly by energetic electrons which are treated separately. The basic idea is that

the classical mean free path is much longer than any characteristic scale length. For instance if $T_e =$ 10 keV and $n = 10^{21}$ cm^{-3}, the electron mean free path is roughly one millimeter. Thus a classical fluid model is not valid for these electrons. However separate transport of these electrons is a very complicated procedure and to our knowledge, there is no generally agreed upon procedure for it.

The approach that we adopt is very different. We use a single fluid model and justify it by a large anomalous collision frequency. For instance, if the return current excites an ion acoustic instability with fluctuation amplitude $e\phi/T_e$, the anomalous collision frequency is given roughly by $\omega_{pe} (e\phi/T_e)^2$. Therefore, if $e\phi/T_e \sim 10^{-1}$ the electron mean free path for a 10 keV plasma at $n = 10^{21}$ cm^{-3} is roughly 2 microns. Thus a single fluid approximation is now much more reasonable. Even if the absorption process gives rise to nonthermal electron distributions (for instance resonant absorption almost certainly does[8-11]), if the transport of these energetic electrons is inhibited, a single fluid theory is probably still valid everywhere except right at the position where the nonthermal electrons are accelerated. At these points the thermal temperature we calculate will be some average of the superthermal and thermal temperature actually produced.

Thus our philosophy is to explore the consequences of a single fluid description of the electrons and see where it leads. For one thing we find that the temperature in the underdense plasma is generally much greater than the thermal electron temperature predicted by LASNEX. Our thermal temperature in the underdense region, in fact agrees much better with both the superthermal electron energy of the LASNEX simulations and shown by experiment. Of course there will still be runaway tails on the electron distribution function, but now they perturb rather than dominate the electron transport. We find that this model does give reasonable results. Another great advantage is that it is a very straightforward theory and is very economical to study.

A2. Conclusions

We conclude that fluid simulations with anomalous transport, is an accurate and cost effective way to describe the absorption, backscatter and flux limitation in a laser produced plasma. Our calculations

9

give quantitatively correct absorption of laser light over five orders of magnitude in irradiance, for short pulses, long pulses, and double structured pulses. It has been shown that reducing the laser wavelength is favorable to absorption of laser light by targets (although it might not be overall more efficient). Another important result uncovered by this work is that the physics of absorption is different for short and long pulses at high intensities ($\phi\lambda^2 > 10^{14}$ W/cm$^2-\mu^2$). This has been confirmed recently in experiments.[56]

REFERENCES

1. W.M. Manheimer, D.G. Colombant and B.H. Ripin, Phys. Rev. Lett. 38, 1135 (1977).

2. W.M. Manheimer and D.G. Colombant, Phys. Fluids 21, 1818 (1978).

3. B.H. Ripin, F.C. Young, J.A. Stamper, C.M. Armstrong, R. Decoste, E.A. McLean and S.E. Bodner, Phys. Rev. Lett. 39, 611 (1977).

4. B.H. Ripin and E.A. McLean, NRL Memo Report 3964 (1979); to be published in Appl. Phys. Lett.

5. B.H. Ripin, R.R. Whitlock, F.C. Young, S.P. Obenschain, E.A. McLean and R. Decoste, NRL Memo Report 3965 (1979); B.H. Ripin, R. Decoste, S.P. Obenschain, S.E. Bodner, E.A. McLean, F.C. Young, R.R. Whitlock, C.M. Armstrong, J. Grun, J.A. Stamper, S.H. Gold, D.J. Nagel, R.H. Lehmberg, and J.M. McMahon, to be published in Phys. Fluids.

6. B.H. Ripin, NRL Memo Report 3684 (1977).

7. C.G.M. Van Kessel, J.N. Olsen, P. Sachsenmaier, R. Sigel, K. Eidmann and R.P. Godwin, presented at the 10th European Conf. on Laser Interaction with Matter, Ecole Polytechnique, Palaiseau, France (1976).

8. J.P. Freidberg, R.W. Mitchell, R.L. Morse and L.J. Rudinski, Phys. Rev. Lett. 28, 795 (1972).

9. D.W. Forslund, J.M. Kindel, K. Lee, E.L. Lindman and R.L. Morse, Phys. Rev. A **11**, 679 (1975).

10. K.G. Estabrook, E.J. Valeo and W.L. Kruer, Phys. Fluids **18**, 1151 (1975).

11. D.W. Forslund, J.M. Kindel and E.L. Lindman, Phys. Fluids **18**, 1017 (1975).

12. R.A. Haas, W.C. Mead, W.L. Kruer, D.W. Phillion, H.N. Kornblum, J.D. Lindl, D. McQuigg, V.C. Rupert, and K.G. Tirsell, Phys. Fluids **20**, 322 (1977).

13. H.D. Shay, R.A. Haas, W.L. Kruer, M.J. Boyle, D.W. Phillion, V.C. Rupert, H.N. Kornblum, F. Rainer, V.W. Slivinsky, L.N. Koppel, L. Richards, and K.G. Tirsell, Phys. Fluids **21**, 1634 (1978).

14. M.D. Rosen, D.W. Phillion, V.C. Rupert, W.C. Mead, W.L. Kruer, J.J. Thomson, H.N. Kornblum, V.W. Slivinsky, G.J. Caporaso, M.J. Boyle and K.G. Tirsell, Preprint UCRL-82146 (1978).

15. G. Zimmerman and W.L. Kruer, Comm. Plasma Phys. **2**, 85 (1975); G.B. Zimmerman, Lawrence Livermore Laboratory Report No. UCRL-74811, 1973 (unpublished).

16. W.M. Manheimer, Phys. Fluids **20**, 265 (1977).

17. W.M. Manheimer, C.E. Max, and J.J. Thomson, Phys. Fluids **21**, 2009 (1978).

18. R. Faehl and W.L. Kruer, Phys. Fluids **20**, 55 (1977).

19. A. Mase and T. Tsukishima, Phys. Fluids **18**, 464 (1975).

20. C.C. Daughney, L.S. Holmes and J.W.M. Paul, Phys. Rev. Lett. **25**, 497 (1970).

21. K. Muraoka, E.L. Murray, J.M.W. Paul and D.R. Summers, J. Plasma Phys. **10**, 135 (1973).

22. Y. Kowai and M. Guyot, Phys. Rev. Lett. **39**, 1141 (1977).

23. S.M. Hamburger and J. Jancarik, Phys. Fluids **15**, 825 (1972).

24. R.E. Slusher, C.M. Surko, D.R. Moler and M. Porkolab, Phys. Rev. Lett. **36**, 674 (1976).

25. A.Y. Wong, B.H. Quon and B.H. Ripin, Phys. Rev. Lett. **30**, 1299 (1973).

26. B.H. Quon, A.Y. Wong and B.H. Ripin, Phys. Rev. Lett. **32**, 406 (1974).

27. M. Lampe, W.M. Manheimer, J.B. McBride, J.H. Orens, R. Shanny, and R. Sudan, Phys. Rev. Lett. **26**, 1221 (1971).

28. M. Lampe, W.M. Manheimer, J.B. McBride, J.H. Orens, K. Papadopoulos, R. Shanny and R.N. Sudan, Phys. Fluids **15**, 662 (1972).

29. M. Lampe, W.M. Manheimer, J.B. McBride, and J.H. Orens, Phys. Fluids **15**, 2356 (1972).

30. M. Lampe, I. Haber, J.H. Orens and J.P. Boris, Phys Fluids **17**, 428 (1974).

31. J.A. Wesson, A. Sykes and H.R. Lewis, Plasma Phys. **15**, 49 (1973).

32. D. Biskamp and R. Chodura, Phys. Fluids **16**, 893 (1973).

33. D. Biskamp, K.U. von Hagenow and H. Welter, Phys. Lett. **39A**, 351 (1972).

34. C.T. Dum, Phys. Fluids **21**, 956 (1978).

35. M.Z. Caponi and R.C. Davidson, Phys. Rev. Lett. **31**, 86 (1973).

36. A.M. Sleeper, J. Weinstock and B. Bezzerides, Phys. Fluids **16**, 1508 (1973).

37. W.M. Manheimer and R. Flynn, Phys. Fluids **17**, 409 (1974).

38. D. Choi and W. Horton, Phys. Fluids **17**, 2048 (1974).

39. M.N. Rosenbluth, Phys. Rev. Lett. **29**, 565 (1972).

40. K. Nishikawa and C.S. Liu in *Advances in Plasma Physics,* Vol. 6 Wiley & Sons (1976).

41. M.N. Rosenbluth, R.P. White, and C.S. Liu, Phys. Rev. Lett. **31**, 1190 (1973).

42. W.M. Manheimer, Phys. Fluids **17**, 1634 (1974).

43. D.W. Phillion, W.L. Kruer, and V.C. Rupert, Phys. Rev. Lett. **37**, 1529 (1977).

44. C.L. Tang, J. Appl. Phys. **38**, 390 (1967).

45. W.M. Manheimer and H.H. Klein, Phys. Fluids **17**, 1889 (1974).

46. P.M. Campbell, R.R. Johnson, F.J. Mayer, L.V. Powers, and D.C. Slater, Phys. Rev. Lett. **39**, 274 (1977); R.L. Morse and R.C. Malone, Bull. Am. Phys. Soc. **21**, 1028 (1976).

47. J.M. Dawson and C. Oberman, Phys. Fluids **6**, 394 (1963).

48. K. Lee, D. Forslund, J.M. Kindel and E.L. Lindman, Phys. Fluids **20**, 51 (1977).

49. B.H. Ripin, Appl. Phys. Lett. **30**, 136 (1977).

50. F.C. Young and B.H. Ripin, Bull. Am. Phys. Soc. **22**, 1112 (1977), submitted for publication.

51. J.P. Anthes, M.A. Palmer, M.A. Gusinow and K.M. Matzen, Bull. Am. Phys. Soc. **23**, 777 (1978).

52. F. Amiranoff, R. Benattar, R. Fabro, E. Fabre, C. Garban, C. Popovics, A. Poqueruse, R. Sigel, C. Stenz, J. Virmont and M. Weinfeld, in Plasma Physics and Controlled Thermonuclear Fusion (International Atomic Energy Agency, Vienna, 1978) (to be published).

53. M. Read. R. Gilgenbach, R. Lucey, K.R. Chu and V.L. Granastein, to be published.

54. K.R. Manes, V.C. Rupert, J.M. Auerbach, P.H.Y. Lee, and J.E. Swain, Phys. Rev. Lett. **39**, 281 (1977).

55. NRL Laser-Plasma Interaction Group, NRL Memo Report 3890 (1978), ed. B.H. Ripin.

56. B. Arad, S. Eliezer, S. Jackel, A. Krumbein, H.M. Loebenstein, D. Salzmam, A. Zigler, H. Zmora, and S. Zweigenbaum, Phys. Rev. Lett. **44**, 326 (1980).

B1. Energy Conversion of Light Ion Beams by Ablative Acceleration of Thin Foils

Light ion beams provide a power source of longer pulse duration than that typical of laser power sources. This source in turn calls for larger size, thin shell pellet designs for inertial confinement fusion. The optimum thickness of the foil for conversion of beam energy to kinetic energy of the target payload depends on making the foil sufficiently thick to stop the beam completely and maintain target integrity during beam absorption while keeping the mass of the payload to a minimum, maximizing the final velocity achieved.

We report here the results of a numerical investigation of the accelerations of a variety of thicknesses of thin gold foils by a 1.4 Mev proton beam. The proton beam is simulated by a time-dependent monoenergetic beam of parallel protons. The time history of the energy and current per square centimeter of the beam shown in Fig. B1.1 corresponds to the beam produced experimentally in the Gamble II facility at NRL. It is modeled by linear segments with a maximum beam energy of 1.4 Mev and maximum beam current of 450 kA/cm^2. this corresponds to a maximum beam power of 6.3 × 10^{11} watts/cm^2. The current pulse length is 65 ns which results in a total energy in the beam over the pulse of 19.4 KJ/cm^2.

The target consists of a uniform plane gold foil with a parallel proton beam impinging from the right. The convention will be used that the front side of the foil is the side on which the proton beam impinges. The numerical simulations are done for a uniform slab of thickness ranging from 7.5μ to 20μ. The 1.4 Mev proton beam has a range of 10μ in the cold gold foil so that the foil thickness ranges from subrange to twice the beam range in the foil.

The numerical simulations were carried out using a quasi-Lagrangian one-dimensional hydro code in slab geometry. The essential features of the code are outlined in Fig. B1.2. The code solves the

14

conservation equations for mass, momentum and energy with a flux conserving numerical scheme. The interfaces with the free boundaries on either side are treated in a fully Lagrangian manner. The regions between the two outer interfaces are treated using the moving zone flux-corrected transport (FCT) algorithms. The zones are moved in such a way that the mass per unit zone is approximately constant. The code incorporates a single fluid, two-temperature (electron and ion) model with an independent electron energy transport equation. The ion temperature is found by subtracting the electron and kinetic energies from the total energy. Classical electron and ion thermal conductivities are treated in an implicit conduction routine along with the equilibration terms. In the runs to be described here the electrons and ions are constrained to have the same temperature assuming local thermodynamic equilibrium. Radiation transport is treated using the radiation conduction approximation in the optically thick region where local thermodynamic equilibrium is assumed. The optically thin regions are treated using a volume of emission coefficient. The transition from thick to thin is assumed to take place one optical depth from each of the free surfaces. The brightness temperature is calculated based on the integrated radiation from each side. The last thick cell on each side is limited by black body radiations from that cell.

The equation of state of the hot gold plasma is calculated from curve fits to the Saha equilibrium calculations for gold. At low temperatures the solid material properties of the gold are included from empirical curve fits to the cold compression curves and using a Grüneisen coefficient for the thermal component. The equation of state is matched at the low-temperature, high density limit to the Thomas-Fermi-degenerate electron limit and at high temperatures and low densities to the Saha equilibrium limit.

The ion beam deposition is treated in two parts. The slowing down due to bound electrons is treated using an empirical experimentally determined range energy-relation to determine the slowing down rate as a function of beam energy and target density. This determines the cold slowing down formulae. To this is added a correction as the gold becomes ionized for the bound ionization potential and due to the slowing down due to free electrons which are treated classically.

15

The results may be summarized in Figs. B1.3 and B1.4. In Fig. B1.3 we show the asymptotic distribution of energy of the gold foil as a function of the foil thickness (after it has expanded to low pressure). This is the measure of how the beam energy will be distributed after the foil has accelerated to maximum velocity. The payload kinetic energy is defined as the energy of all the gold material moving in the direction away from the beam source. It shows a broad maximum in the range of $10\text{-}15\mu$ gold thickness. Below 10μ not all of the beam energy is absorbed as it is insufficiently thick to stop the beam. Above 15μ it begins to fall off as the increased mass of the payload reduces the final maximum velocity obtained. The total momentum delivered to the payload remains nearly constant as a function of foil thickness once the beam is totally absorbed, thus the increased mass results in a lower payload velocity. The internal energy includes both thermal and ionization energy and increases only slowly with increased foil thickness representing about 12% of the total energy. The radiated energy increases at first as more of the beam energy is absorbed but then decreases when the foil becomes thicker than the beam range since it radiates from one side only until the thermal wave burns through to the back surface. This takes longer with the thicker foil and after the beam shuts off the foil cools due to adiabatic expansion before burning through, thus radiating less. Most of this energy is recovered in kinetic energy of the foil material as can be seen by the rapid rise in total kinetic energy. However, most of the kinetic energy is carried off with the ablating foil material, hence the broad flat peak in the payload kinetic energy. The increased energy available from the lowered radiated energy balances the decrease in payload kinetic energy due to the increasing mass of the payload. The result is a broad peak where a broad peak where about 27% of the beam energy has been converted to payload kinetic energy moving at an average velocity of about 2×10^6 cm/sec.

In Fig. B1.4 we show the brightness temperature of the front and back sides of the foil. Also shown is the peak temperature anywhere in the foil as a function of foil thickness. This temperature rises slowly with increased foil thickness as the result of the more massive foil remaining intact longer reducing the cooling from adiabatic expansion. The brightness temperature is a measure of the total radiation from an optically thick plasma. This figure demonstrates the dramatic drop in radiation from

16

the back surface as the foil thickness exceeds the range of the ion beam. When the ion beam no longer penetrates to the back surface no radiation takes place until a thermal wave from the hot plasma interior burns through to the surface. As the foil becomes thicker this takes a longer time and the plasma interior begins to cool by adiabatic expansion and radiation on the front side before the wave can burn through, thus the back surface will radiate at a much lower temperature and for a shorter period of time.

In Figs. B1.5 to B1.7 we show the velocities and temperatures of the front and back surface as a function of time. Plotted is the velocity of the leading edge of the front side and the negative of the back side velocity. Also shown is the mean velocity of the payload which is defined as the total momentum of material moving in the direction away from the beam divided by the mass of this material. The closer this velocity is to the back side edge the more nearly the payload is being accelerated as an intact foil. In the 7.5μ case shown in Fig. B1.5 the ion beam penetrates to the back side edge and accelerates it to high velocity. If we look at the temperature of the back side, it does not begin its rapid rise until about 12 ns. This is the result of using the ramp profile in time for the beam energy. The early portion of the beam does not have sufficient energy to penetrate the foil. Note that the peak temperature occurs at about 45 ns which is the time of peak ion beam power. In Fig. B1.6 we see the results for a foil thickness of 12.5μ which is somewhat greater than the proton beam range. Note that for the first 20 ns the leading edge and average velocities are nearly the same since the accelerated leading edge remains a solid. At about 25 ns a thermal wave from the hot interior reaches the back surface accompanied by a rapid increase in the brightness temperature and a rapid acceleration of the back edge as the surface vaporizes and blows off. This rapid expansion results in a cooling which can be seen by the lowering of the radiation temperature. At later times a second thermal wave catches up with the leading edge causing another rise in the surface temperature. In addition, as the density of the leading edge drops, the outer plasma becomes optically thin and radiation from the hotter interior escapes. Note also, as in the 7.5μ case, most of the acceleration takes place while the ion beam is irradiating the target. Since the foil becomes completely vaporized the leading and trailing edges both have

much greater velocity than the mean payload velocity. For the 20μ foil case shown in Fig. B1.7 the foil is sufficiently thick that the thermal wave does not arrive at the front surface until after the proton beam has ended and is at a much lower temperature. Note that the mean velocity and the leading edge velocity remain nearly the same indicating acceleration at near solid density. A weak shock arrives at the leading edge at about 30 ns but is insufficient to vaporize the gold material yielding only an increased acceleration of the leading edge. The thermal wave which finally reaches the leading edge at about 75 ns is much colder than the others since the plasma has begun to cool before it reaches the leading edge. The front side temperature and leading edge velocity are relatively the same for each case. This yields the result that the momentum transferred to the payload is nearly constant. The velocity and kinetic energy decrease as the mass of the payload increases.

The results of these calculations indicate that at least at these power levels an ion foil can be accelerated with greater than 25% efficiency in conversion of beam energy to kinetic energy of the moving foil. The acceleration is ablative as can be seen by the fact that most of the foil acceleration takes place while the beam power is on, and the results indicate that the rocket model where the momentum transfer is proportionate to the ablated mass and ablation velocity is applicable for the ion beam acceleration. Since the ion beam penetrates approximately a constant mass of material for a uniform beam energy, the results indicated that most of the ablation mass is contained in the region the beam has penetrated and little additional mass is ablated from the penetration of the thermal wave.
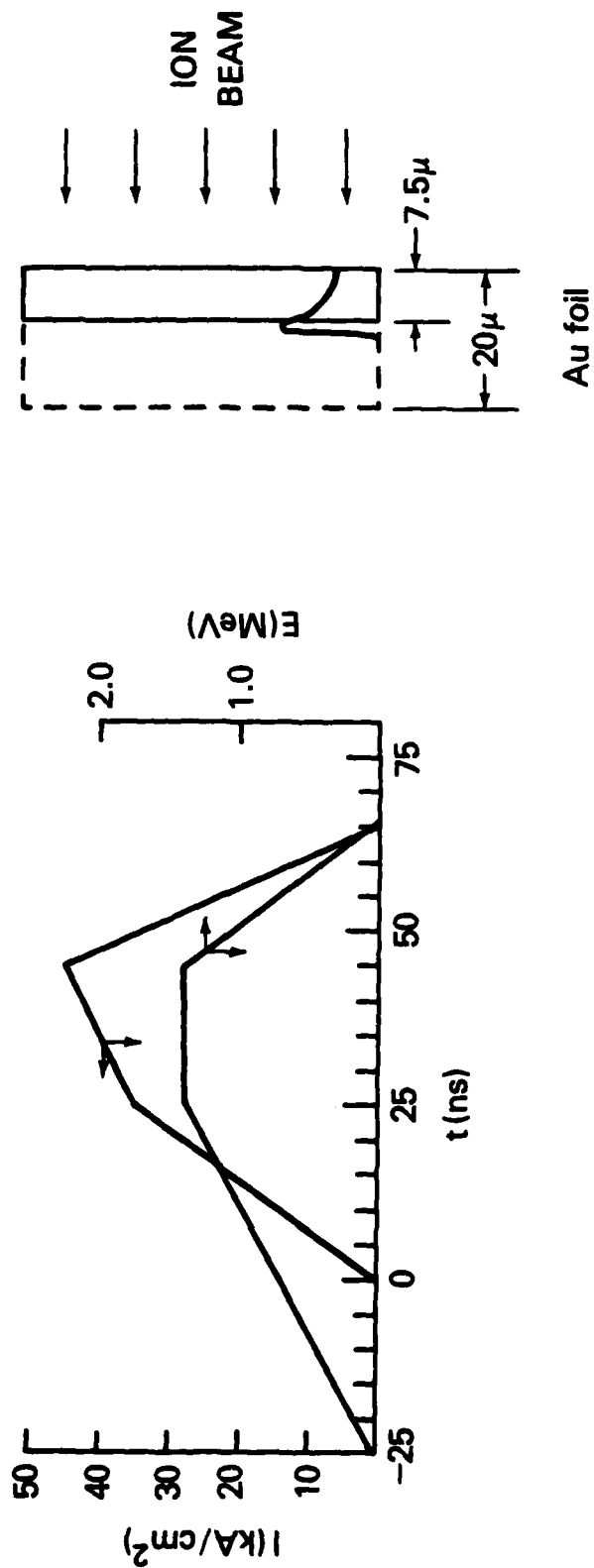
ION BEAM PROFILE

Fig. B1.1 — Ion Beam current and voltage profiles as a function of time. Zero time corresponds to start of beam deposition. Diagram at right shows schematic of beam deposition profile in cold gold foil.

FCT ONE-DIMENSIONAL HYDROCODE

- Solves fully conservative equations with a flux-conserving numerical scheme in either slab, cylindrical, or spherical geometry.

- Interfaces between materials and free boundaries are fully Lagrangian with arbitrary numbers of interfaces.

- Regions between interfaces are treated with moving zone flux-corrected transport (FCT).

- Two-temperature model (T_e, T_i) is used with implicit thermal conduction and equilibration (classical coefficients with flux limiting).

- Radiation transport uses conduction approximation in optically thick regions and volume emission in thin regions with transition at one optical depth from surface.

- Equation-of-state treats solid material properties and Ferm-degenerate electrons at high densities with ionization state determined by Saha equilibrium.

- Ion beam deposition uses empirical range energy relation for bound electrons and classical slowing down for free electrons.

Fig. B1.2 — Essential features of the Quasi-Lagrangian one-dimensional hydro code in slab geometry.
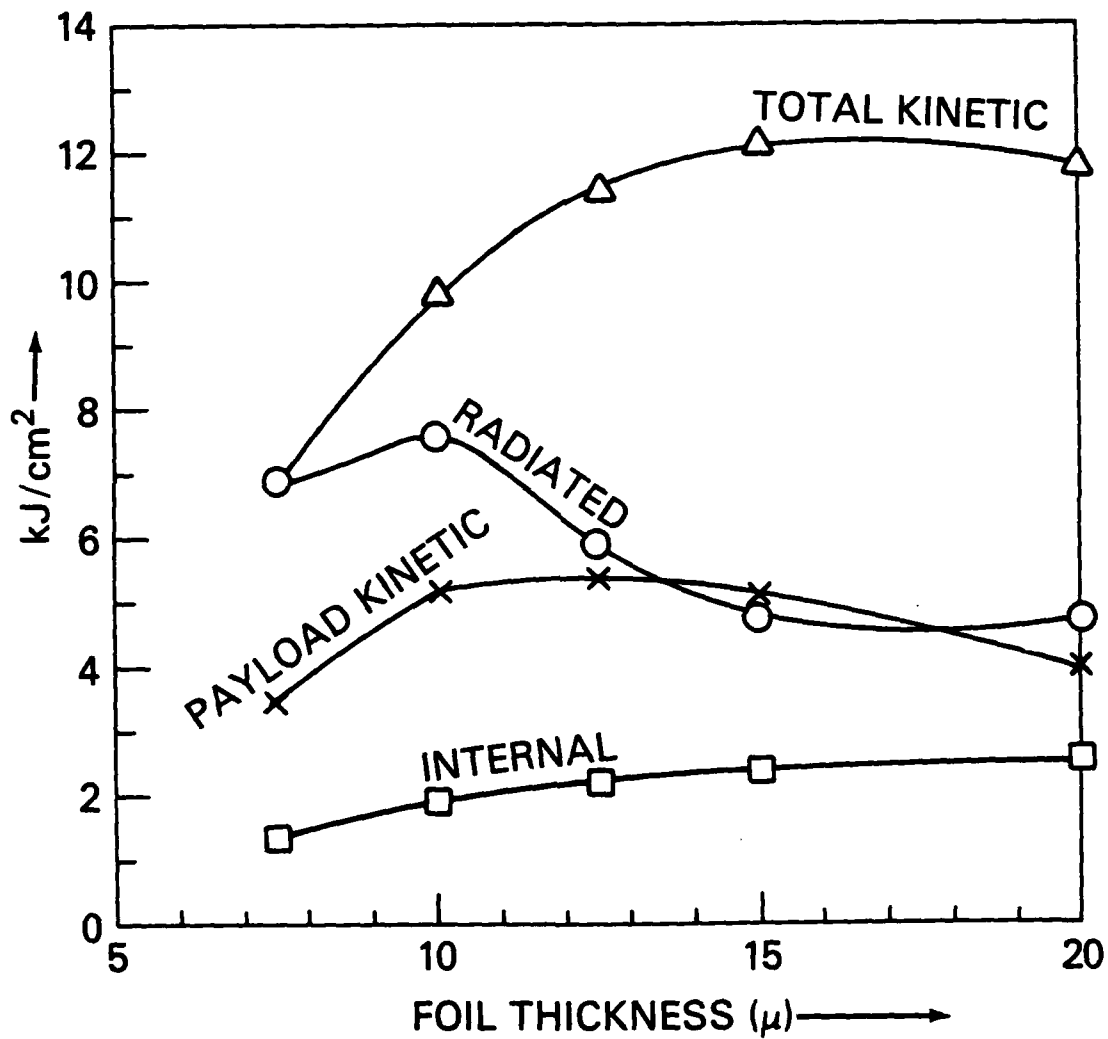
ION-FOIL ENERGY BUDGET

Fig. B1.3 — Distribution of energy after foil has expanded for 150 ns. Payload kinetic energy peaks at a foil thickness that approximately corresponds to the ion beam range in cold gold.
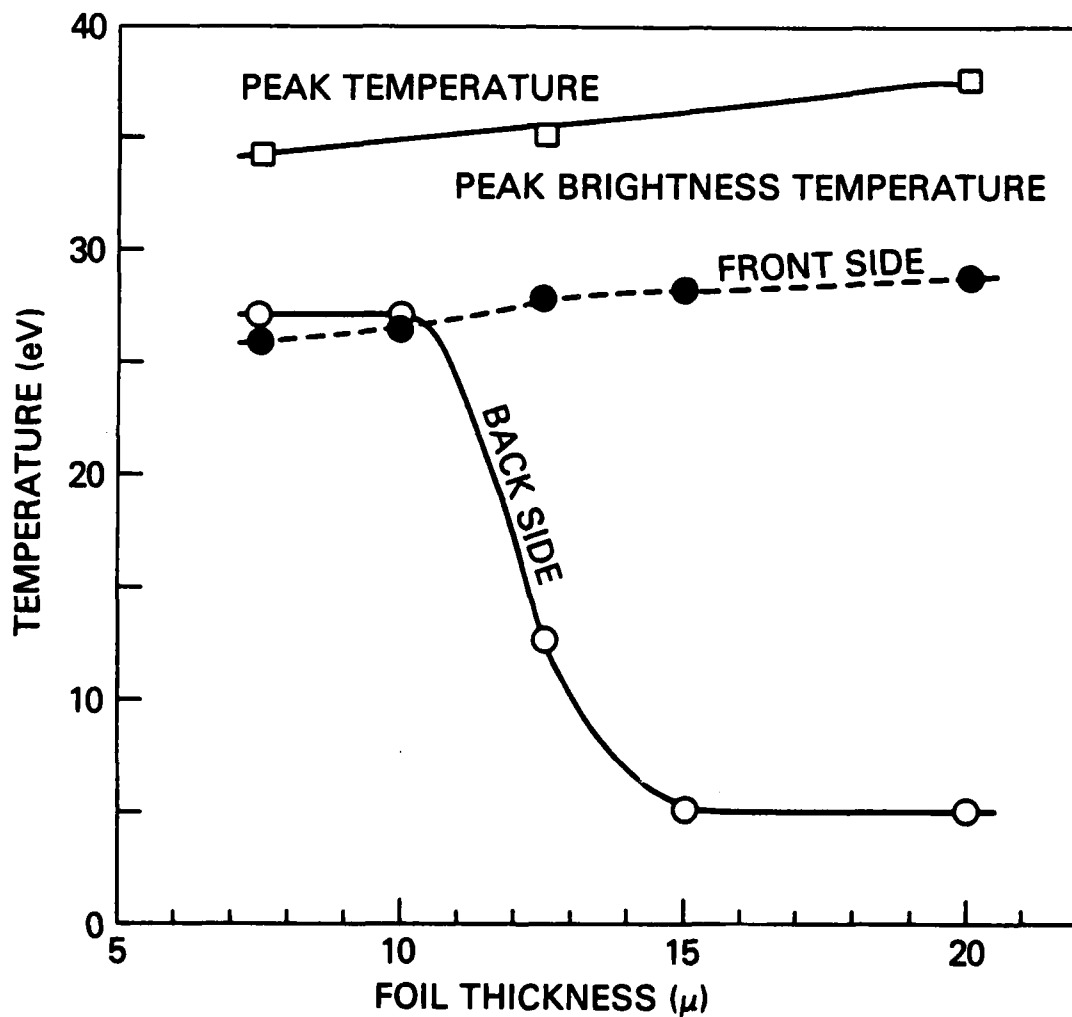
21

ION-FOIL TEMPERATURE

Fig. B1.4 — Peak temperature of an equivalent black body radiation from the front and rear surfaces. Rapid drop on rear surface occurs when foil thickness is greater than the ion beam range.
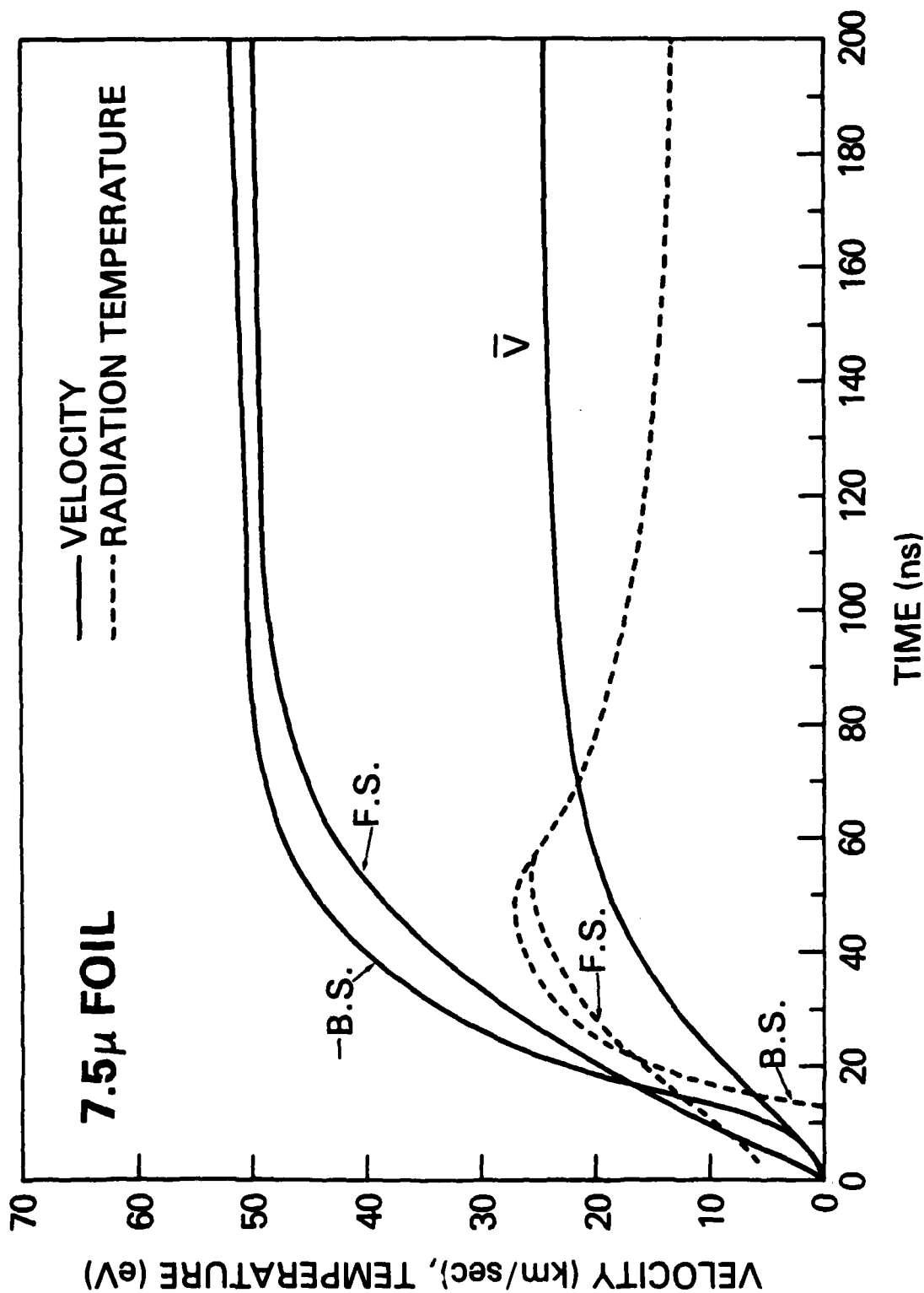
Fig. R1.5 — Velocity and temperature of front and rear surfaces. $\bar{V}$ corresponds to the average velocity of the payload as distinct from the back surface edge velocity.
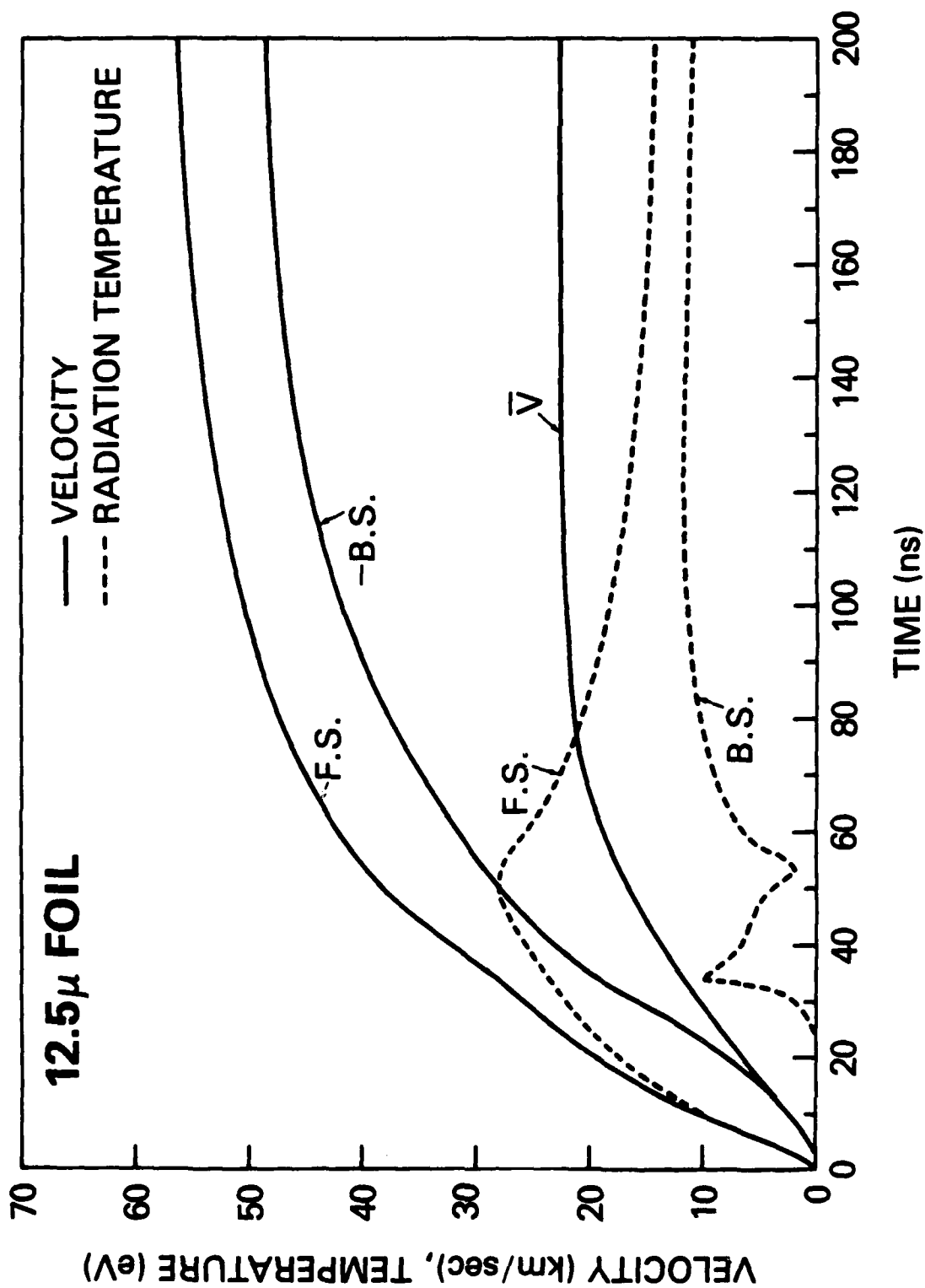
Fig. B1.6 — Velocity and temperature of front and rear surfaces. The double peaks in back side radiation temperature is caused by expansion of back surface after the thermal wave reaches it.
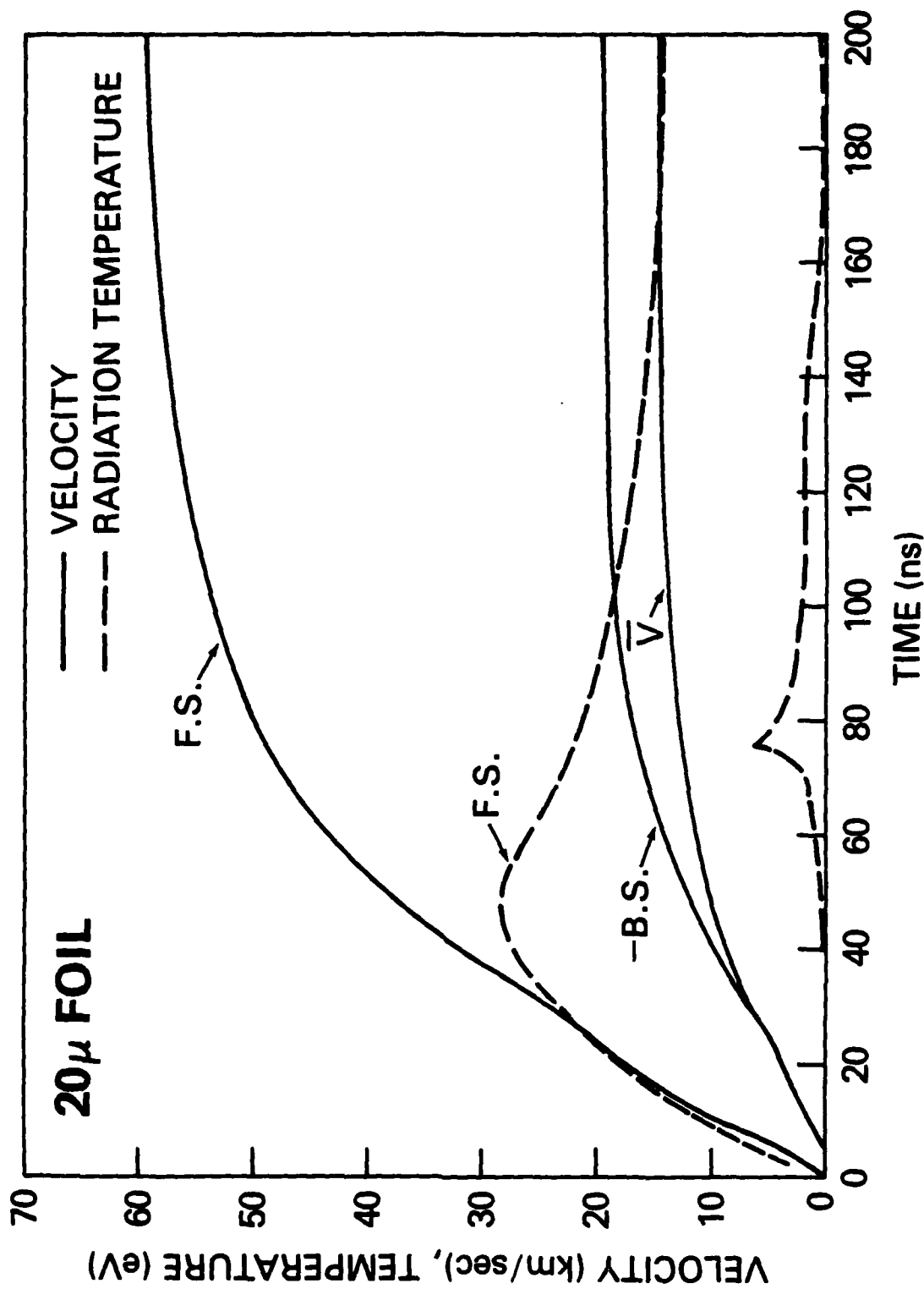
Fig. B1.7 — Velocity and temperature of front and rear surfaces. The average velocity and back side velocity are nearly the same as long as the foil remains solid until it is heated sufficiently to vaporize.

B2a. Spherical Shock Implosion Dynamics and Stability

One of the critical limitations to achieving a high degree of compression in a spherical implosion is the degree of symmetry that can be maintained during the implosion process. Several procedures are available to help analyze the issues of the stability and symmetry in implosions involving both analytic and numerical treatment. The simplest of these involves linearized perturbation analysis of some zero order spherically symmetric solution to determine if the solution is stable. If it is not, multidimensional calculations are required to estimate how large the perturbations become and if there is a saturation mechanism. Rayleigh-Taylor modes in a laser-driven ablation layer have been analyzed extensively at NRL in this manner.

The zero order solution may be found either analytically using some self-similar solution, or numerically. The perturbations also may be investigated either analytically or numerically leading to the so-called "piggy-back" methods. A complementary approach to finding the growth of linearized unstable modes is the direct numerical solution of the multi-dimensional fluid equations. In this approach the solutions are found without perturbation analysis at the expense of a rather large hydrodynamics calculation to be performed for each set of parameters to be investigated. Modes of a few zone sizes are the smallest that can be investigated in a detailed multidimensional simulation. This approach requires rather fine gridding and expensive calculations to look at short wavelength phenomena.

One of the important issues in understanding imploding systems is the stability of a converging shock wave. This shock might be used, for instance, not only to compress the fuel, but also to provide the required heating to create a central ignition region. The final temperature achievable will depend on how spherical the shock wave remains during the collapse process and the shape of the shock at the time of reflection.

The motion of a converging shock wave can be computed with great accuracy by considering only the changes in the physical variables across the shock front, ignoring the motion behind the shock front. The shock front moves normal to the shock surface so it may be treated as locally one-

26

dimensional flow down a channel whose boundaries are determined by the trajectories of the shock front. These trajectories form imaginary ray tubes whose cross-sectional area may be related to the Mach number by an equation developed by Chester-Chisnell-Whitham (CCW approximation)[1-3]

$$\frac{\lambda(M)M^2}{M^2 - 1} \frac{dM}{M} + \frac{dA}{A} = 0, \quad \text{where}$$

$$\lambda(M) = \left[2\sigma + 1 + \frac{1}{M^2}\right]\left[1 + \frac{2}{\gamma + 1} \frac{1 - \sigma}{\sigma}\right] \text{ and } \sigma = \frac{(\gamma - 1)M^2 + 2}{2\gamma M^2 - (\gamma - 1)} \quad (1)$$

This approximation allows a great deal of savings in computational time and storage since one needs only store the location and Mach number of the shock front and compute the trajectory of the shock front rather than the entire flow field. The problem can be reduced to the calculation of a set of ordinary differential equations for the trajectories of a finite number of points located along the shock front and for their associated time-dependent Mach numbers.

A code based on this approximation has been written and enables us to investigate a wide range of stability and symmetry issues related to shock collapse. For instance, there is the question of how large the initial perturbations may be even for stable modes since the perturbation amplitude may not go to zero as fast as the average radius. The concept of stability in the sense of a growing or decaying perturbation does not make much sense for this particular problem. Given a set of wavelengths, Mach number, and initial radius, can the collapse of the shock be timed so that the mode amplitude of an oscillating perturbation is zero at the time of collapse? Is there a cutoff mode number below which the wave front becomes more rather than less spherical during collapse?

In order to address these questions we have developed a code similar to that of Fong and Ahlborn[4]. The motion of the shock front is described by K mesh points whose equation of motion is given by:

$$X_k^{n+1} = X_k^n + M_k^{n+1/2} \cos\left(N_k^{n+1/2}\right)a\left(t^{n+1} - t^n\right) \quad (2a)$$

$$Y_k^{n+1} = Y_k^n + M_k^{n+1/2} \sin\left(N_k^{n+1/2}\right)a\left(t^{n+1} - t^n\right) \quad (2b)$$

where (X_k^n, Y_k^n) is the Cartesian coordinate of the kth mesh point at the nth time interval; $M_k^{n+1/2}$ is the Mach number at $(X_k^{n+1/2}, Y_k^{n+1/2})$, $N_k^{n+1/2}$ is the angle between the shock and the axis, a is the sound speed ahead of the shock, and t the time. The $n+1/2$ values are formed by advancing the equations for half a

timestep to make the overall algorithm second order. The angle factors are evaluated by averaging the angles formed by joining the adjacent mesh points with straight lines.

$$\cos(N_k^n) = \frac{\cos(N_{k+\frac{1}{2}}^n) + \cos(N_{k-\frac{1}{2}}^n)}{2} = -\frac{Y_{k+1}^n - Y_k^n}{2r_{k+\frac{1}{2}}^n} - \frac{Y_k^n - Y_{k-1}^n}{2r_{k+\frac{1}{2}}^n} \tag{3a}$$

$$\sin(N_k^n) = \frac{\sin(N_{k+\frac{1}{2}}^n) + \sin(N_{k-\frac{1}{2}}^n)}{2} = \frac{X_{k+1}^n - X_k^n}{2r_{k+\frac{1}{2}}^n} + \frac{X_k^n - X_{k-1}^n}{2r_{k+\frac{1}{2}}^n} \tag{3b}$$

where

$$r_{k+\frac{1}{2}}^n = [(X_{k+1}^n - X_k^n)^2 + (Y_{k+1}^n - Y_k^n)^2]^{\frac{1}{2}}. \tag{4}$$

The mach number is given from the CCW approximations as:

$$M_k^{n+1} = M_k^n - \frac{(M_k^{n+\frac{1}{2}})^2 - 1}{\lambda(M_k^{n+\frac{1}{2}})M_k^{n+\frac{1}{2}}} \left[\frac{A_{k+\frac{1}{2}}^{n+1} - A_{k+\frac{1}{2}}^n}{2 A_{k+\frac{1}{2}}^{n+\frac{1}{2}}} + \frac{A_{k-\frac{1}{2}}^{n+1} - A_{k-\frac{1}{2}}^n}{2 A_{k-\frac{1}{2}}^{n+\frac{1}{2}}} \right] \tag{5}$$

where the area of the ray tube between mesh points is given by

$$A_{k+\frac{1}{2}}^n = \frac{1}{2}(Y_{k+1}^n + Y_k^n)^\alpha r_{k+\frac{1}{2}}^n \qquad \alpha = \begin{cases} 0 & \text{Cartesian} \\ 1 & \text{Cylindrical} \end{cases} \tag{6a}$$

$$A_{k+\frac{1}{2}}^{n+1} = A_{n+\frac{1}{2}}^n + \frac{\partial A_{k+\frac{1}{2}}^n}{\partial X_{k+1}}(X_{k+1}^{n+1} - X_{k+1}^n) + \frac{\partial A_{k+\frac{1}{2}}^n}{\partial X_k}(X_k^{n+1} - X_k^n) \tag{6b}$$

$$+ \frac{\partial A_{k+\frac{1}{2}}^n}{\partial Y_{k+1}}(Y_{k+1}^{n+1} - Y_{k+1}^n) + \frac{\partial A_{k+\frac{1}{2}}^n}{\partial Y_k}(Y_k^{n+1} - Y_k^n)$$

This gives a second-order space and time centered algorithm which is stable subject to a timestep limit analogous to the Courant condition for the one-dimensional fluid equations. That is

$$\Delta t < b \frac{\min(r_{k+\frac{1}{2}}^n, r_{k-\frac{1}{2}}^n)}{M_k^n a} \tag{7}$$

where b is a numerical factor less than one chosen to prevent nonlinear instabilities from developing. We have used values of $b = .05$. This algorithm allows the propagation of shock-shocks (discontinuities in the slope and mach number along the shock front predicted by the Whitham theory) in either direction since the scheme is centered and symmetric. It is not clear that the algorithm proposed by Fong and Ahlborn accomplishes this. As in the Fong and Ahlborn procedure we found it necessary to redistribute the grid points. This was done not for stablity but to prevent unacceptably short timesteps as the mesh points crowd together near the shock-shock regions. The algorithm used here diffuses the grid points a small amount parallel to the shock front in such a way as to make the distances between

28

grid points more nearly equal. This plays a role similar to that of artificial viscosity in the one-dimensional fluid algorithm or surface tension at an interface.

As a test of the accuracy of the numerical procedure described above, we compared the results of the calculation with that predicted by the self-similar solutions for the collapse of an infinitely strong shock due to Guderley.[5] The self-similar solution predicts a shock position given by $R = A(-t)^{\alpha}$ with with $\alpha = .717$ for a $\gamma = 1.4$ gas given by Guderley. This gives a shock Mach number as a function of radius $\dot{R} = -\alpha A(-t)^{\alpha-1} \sim R^{\frac{\alpha-1}{\alpha}}$. Thus $M \sim R^{\frac{\alpha-1}{\alpha}} = R^{-.3947}$. The CCW approximation for large M gives

$$\frac{dA}{A} = 2\frac{dR}{R} = \left[1 + \frac{2}{\gamma+1}\frac{1-\sigma^2}{\sigma}\right]\frac{(2\sigma+1)M^2+1}{M^2-1}\frac{dM}{M} \text{ with } \sigma = \sqrt{\frac{\gamma-1}{2\gamma}}. \tag{8}$$

This gives $M \sim R^{-\frac{2\gamma\sigma}{(2\sigma+1)(\gamma\sigma+1)}} = R^{-.3941}$. This agrees with the analytic Guderley solution to within .15%. In Fig. B2a.1 we show the results of these models for the spherical convergence of a shock with an initial mach number of 57 at a radius of .112 cm. the solid line is the analytic result of the Guderley solution. The triangles are the numerical results of the CCW approximations using the code described above with 25 mesh points around a circle in cylindrical coordinates so that the result describes a spherical implosion. Comparing the results along the axis to those perpendicular to the axis, the shock remains spherical to better than 1% during the entire implosion and the mach number agrees with the Guderley solution with less than .5% error. Since the CCW approximation breaks down as the shock reflects from the origin, it is important to calibrate as well a method capable of computing past the implosion into the explosion phase. The vertical bars are the results computed using the one-dimensional hydrocode FCT1D. The length of the vertical bar represents the uncertainty in the results of the pressure behind the shock due to an uncertainty in its location on a finite grid and the steep pressure gradient behind the shock. These difficulties are one of resolution and can be refined by increased resolution at the expense of computer time and storage.

As a further check on the accuracy of the FCT1D solution, the ratio of the pressure at a given location to the pressure behind the first incident shock at the location is given as a function of the ratio

of time to the time of collapse of that shock and compared to the analytic solution. Since the problem is self-similar, this plot should be the same for all physical locations in space. In Fig. B2a.2 we plot P/P_t vs. $(t - t_c)/(t_o - t_c)$ where the time of collapse t_c has veen taken to be zero. The solid line represents the analytic solution given by Guderley. The horizontal dashed line represents the theoretical jump of 26 behind the reflected shock. The vertical bars with the x's at the end represent the spread in the values found from the numerical results. The uncertainty in the pressure of the numerical results is due to both an uncertainty in the exact location of the incoming shock used to determine the reference shock location (due to the finite width of the shock) and an uncertainty in the exact pressure behind this shock (due to the steep gradient in pressure behind the shock and the finite shock width). The results follow the analytic solution within the accuracy with which they can be interpreted from the numerical solution. This gives us some confidence that the numerical procedure that we are using can accurately determine the solution for the shock collapse problem and subsequent reexpansion with no adjustable parameters needed.

Using the C-C-W code we investigate the stability of a perturbed shock wave. Figures B2a.3 and B2a.4 summarize pictorially the temporal evolution of an 8th order Legendre polynomial perturbation to a spherical shock with amplitude of 5% and 10%, respectively. As the shock collapses toward the origin, the amplitude of the 10% perturbation seems to grow relative to the radius. After implosion by a factor of 5:1, the 10% perturbation goes unstable whereas the 5% perturbation is still behaving within acceptable bounds. Shown is the shape of the shock wave as it collapses from right to left with increasing time.

We also have investigated how symmetric the driver must be in order to produce an imploding shock which is nearly spherical. Using the Chester-Chisnell-Whitham (CCW) approximation we have studied a wide range of stability and symmetry issues related to shock collapse. These yield a set of wavelengths, mach numbers and initial ratio for which the collapse of the shock can be timed so that the amplitude of any particular oscillating perturbation is near zero at the instant of collapse. Superposition of (individually) unstable modes can be stabilized nonlinearly. We have also determined as a

30

function of mode number and initial perturbation amplitude the point at which the growth becomes nonlinear. The stability has been investigated in a special case of the Guderley solution for self-similar spherical shocks imploding into a medium having a power-law density profile. The linearized equations of motion yield an exact solution which predicts power-law growth. This result agrees with that found from the CCW approximation, which has been extended to nonuniform densities.

REFERENCES

1.   W. Chester, Philos. Mag. 45, 1293 (1954).

2.   R.F. Chisnell, Proc. R. Soc. London Ser. A 232, 350 (1955).

3.   G.B. Whitham, J. Fluid Mech. 2, 146 (1957).

4.   K. Fong and B. Ahlborn, Phys. Fluids 22 (3), 416 (1979).

5.   G. Guderley, Luftfarhtforschung 19 (9), 302 (1972).

Spherical Shock Collapse
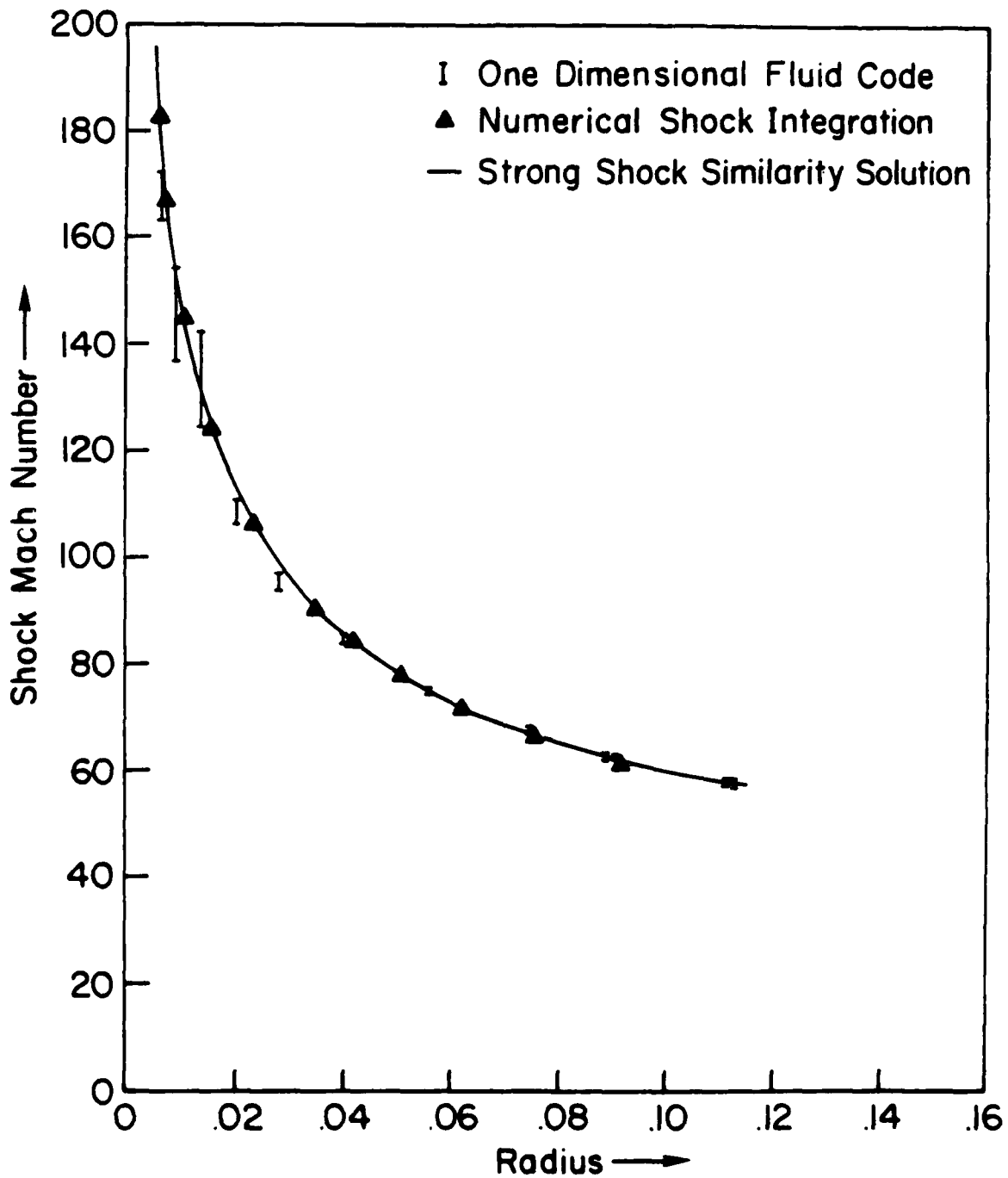
Fig. B2a 1 — Comparison of shock mach number vs radius for three models: (1) Self-similar Guderley solution. (2) Numerical solution of the C-C-W approximation equations. (3) Numerical solution of 1-D fluid equations with FCTID
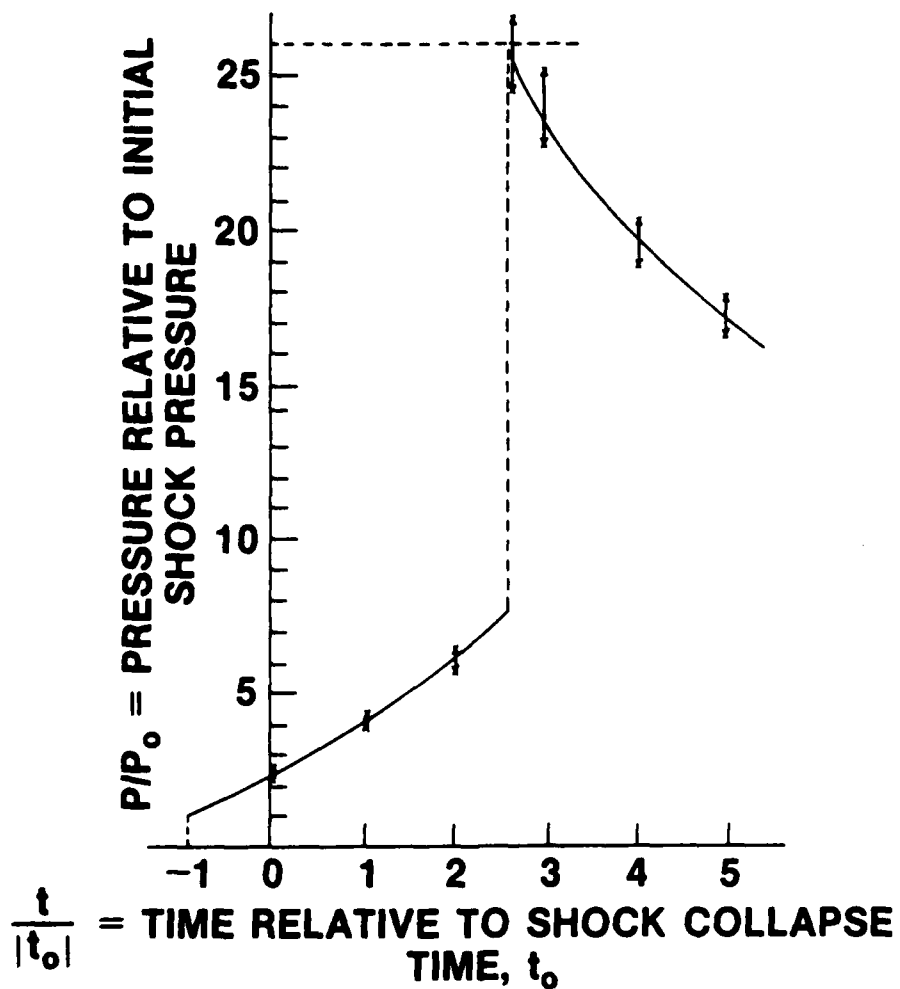
SPHERICAL SHOCK COLLAPSE

Fig. B2a.2 — Comparison of analytic solution due to Guderley with the results of the FCT1D code for the pressure time history of a fixed location during the shock collapse and reexpansion.
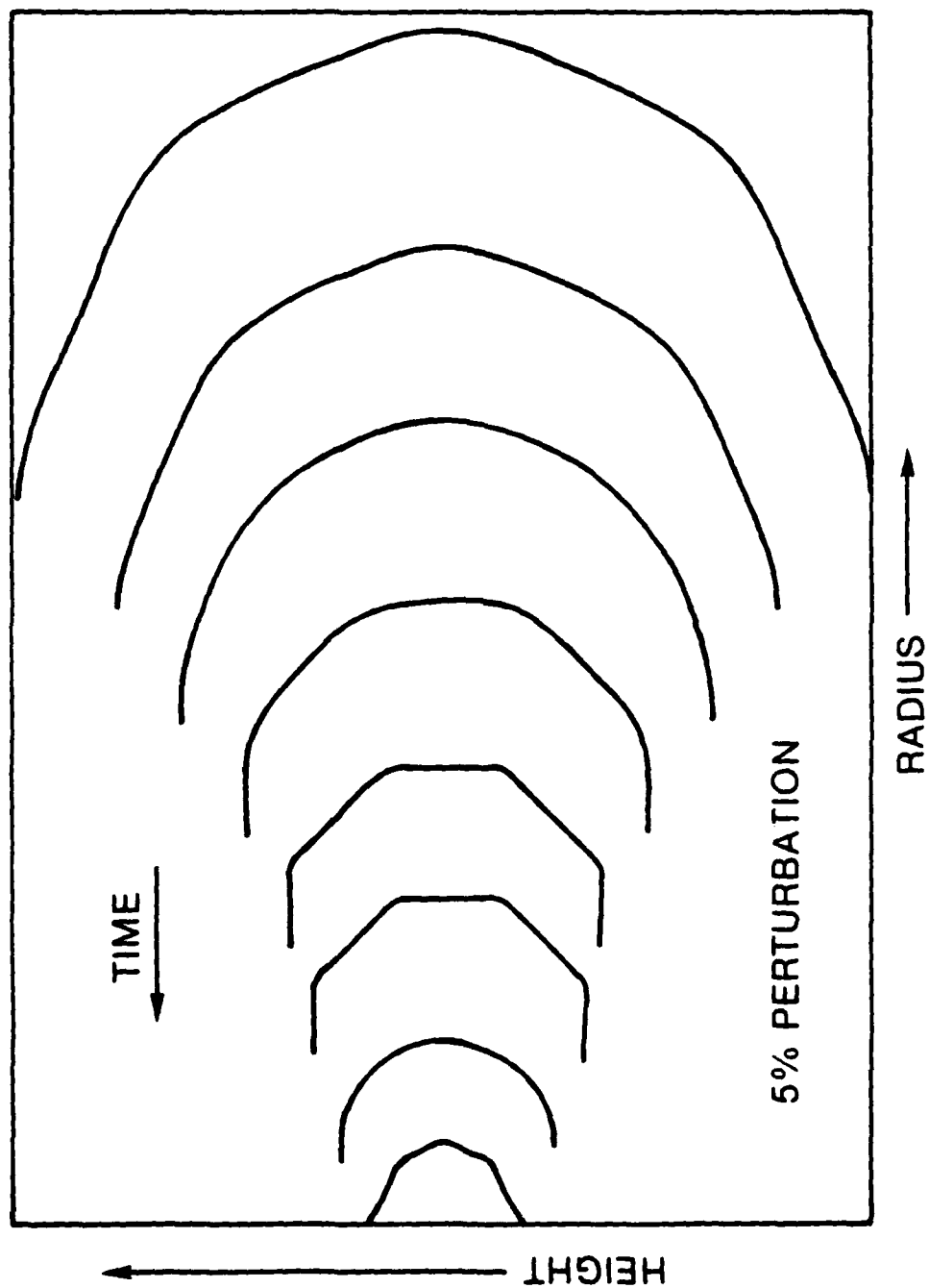
Fig. B2a.3 — Solution using the C-C-W approximation for shock collapse of a spherical shock with an 8th order Legendre polynomial perturbation of 5% amplitude. The perturbation becomes smaller at the same rate as the average radius remaining within acceptable bounds.
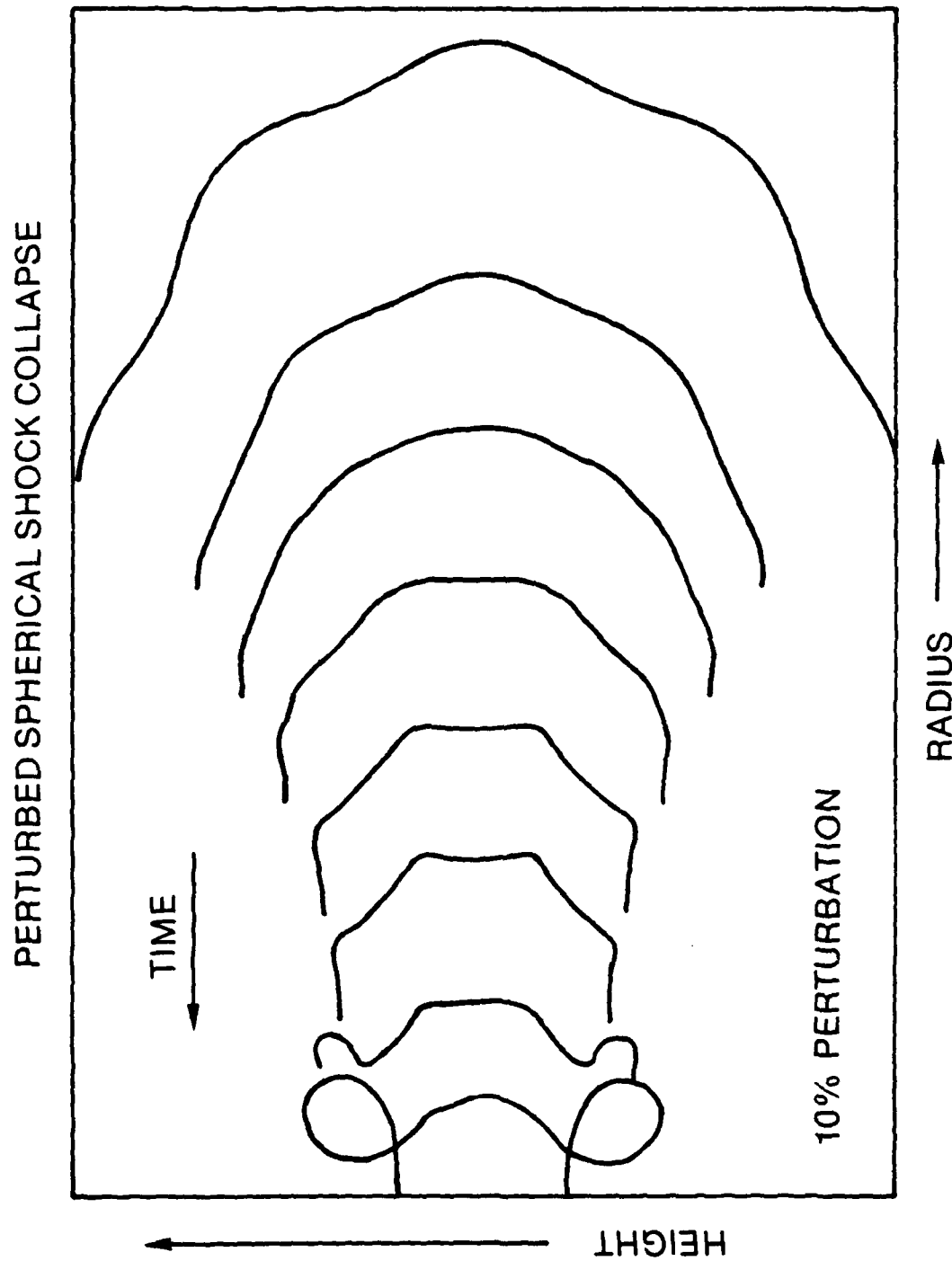
PERTURBED SPHERICAL SHOCK COLLAPSE

TIME

HEIGHT

10% PERTURBATION

RADIUS

Fig. B2a.4 — Solution using the C-C-W approximation for shock collapse with a 10%, 8th order Legendre polynomial perturbation to a spherical shock. The perturbation seems to grow relative to the average radius indicating an unstable behavior.

B2.b Modeling of the Laser Ablation of Thin Foils

It has been demonstrated in a series of experiments at NRL[1] and elsewhere[2] that the use of longer duration and lower intensity laser pulses is useful for achieving successful ablative accelerations in laser-pellet fusion studies. At NRL, a modified version of the Pharos II laser system[3] was used to irradiate thin foil targets of plastic and aluminum. Diagnostics such as interferometry, shadowgraphy, Doppler sounding, calorimetry, and charge collection were used to deduce both target and ablation velocity, mass loss, hydrodynamic efficiency and ablation pressure.[1] These NRL measurements provide a reasonably accurate and complete macroscopic picture of the ablation process, but quantitative microscopic understanding cannot be inferred.

We have analyzed the NRL experiments numerically in order to quantify the controlling physical principles at work in this ablative acceleration and to study the sensitivity of the macroscopic results to plausible variations in the initial transients and the electron thermal conduction transport. The ablative acceleration that results when the longer, lower intensity pulses are used has been the subject of continuing concern.[4]

The 1D computer model used combines a new hydrodynamic package (ADINC)[5] with a classical plasma thermal conduction routine (DIFFU1). The computational grid is Lagrangian, variably-spaced, and rezonable. Since the grid is Lagrangian and the actual problem we wish to consider is time dependent, the initial cell sizes can change in time. In order to prevent cells from becoming either too large or too small, a rezoning package has been included in our program. It is capable of combining neighboring cells while conserving both energy and mass. It also can insert a new cell boundary in regions where either the cells are becoming too large or temperature gradients are to steep. This rezoning allows us to use relatively large time steps (on the average about 8 psec) although the flow velocities are high in the blow-off region (about 6×10^7 cm/sec) and the cell sizes small in the ablation region (about $0.1 \, \mu$).

The 2D code is FAST2D.[6] It uses a sliding Eulerian grid, the Flux-Corrected Transport (FCT) algorithm for solving the hydrodynamic equations, and a two-dimensional classical plasma thermal conduction routine.

For both codes, the thermal conduction coefficient has the classical nonlinear $T^{5/2}$ temperature dependence. We use the standard Braginskii coefficient[7] and assume all plasmas are fully ionized. Also, for the 1D and 2D calculations, the laser flux is introduced as an energy source term in the heat equation and is deposited into the two cells about the critical density. The grid is initially uniform in the region of the foil. Inside and outside of this region the grid is stretched. On the inside (opposite from the laser) this stretched region is filled with a very low density plasma having the same adiabat as the target plasma. On the outside, beyond the critical density, both the density and pressure drop off exponentially.

The initial density, pressure, and temperature profiles are generated from the analytical, quasi-static equilibrium solutions of J. H. Orens.[8] We have shown that these analytic solutions provide an adequate steady state within our 1D computer code. This is done by initializing test runs with these profiles and then proceeding for 1,000 timesteps at constant laser intensity. At the end of these tests only relatively minor changes in the initial profiles have occurred.

Results of our calculations for the standard experimental case of a 15μ thick plastic (CH) foil irradiated by a laser pulse with approximately a 3 nsec fwhm and a peak intensity of 10^{13} w/cm^2 are summarized in Table B2b.I. Here, M_0 is the initial mass of the foil, ΔM is the mass loss, η_h is the hydrodynamic efficiency defined as the final kinetic energy of the foil divided by the total energy absorbed by the target, U is the average ablation velocity, and V is the average target velocity.

Both solutions A and B are initialized at an absorbed laser intensity of 8×10^{11} w/cm^2, corresponding to a time of 3.2 nsec before the peak intensity. We model the time evolution of the laser pulse with a Gaussian having the appropriate width. These two initial quasi-static solutions were

chosen as spanning the kind of different steady state results admissible in our profile generating equations.[8] This ambiguity arises from such things as the choice of the adiabat of the foil and the details of the increase of the laser intensity. The initial density profiles for these two solutions are shown in Fig. B2b.1.

The first four rows of Table B2b.I display the results obtained using the 1D code. Comparing the first and third rows with each other and with the experimental results of the last row, we see that the differences between solution A and B are minimal, and, also, that the agreement with the experimental mass loss and ablation velocity is good. However, both the target velocity and hydrodynamic efficiency are calculated to be too large. This discrepancy arises since we are performing a 1D calculation. In the calculation, all the momentum of the ablated plasma is imparted to the foil. In the experiment, however, the ablated material is seen to emerge in a cone with an opening angle of roughly 20°. Hence, we are overestimating the impulse to the target that the ablated matter transmits and our calculated target velocity and, hence, efficiencies are too high. Results of our simplified 2D calculations will be discussed shortly.

For the 1D calculations, runs where the classical plasma thermal conductivity coefficient was arbitrarily reduced everywhere by a factor of ten were performed. These results are displayed in rows two and four. Somewhat surprisingly, for a factor of ten change in the thermal conductivity, only relatively minor changes occur in the results. As expected, the ablation region becomes hotter and the ablation velocity increases for the lower thermal conductivity case. Also, as expected for this case, less mass is ablated, the ablation is less efficient, and the target achieves a lower velocity.

Part of the reason for this small sensitivity to the thermal conduction coefficient can be deduced from Fig. B2b.2. Here for solution A, the density profiles at the time of peak intensity are displayed for the two different values of thermal conductivity. For the lower value, the density gradients have dramatically steepened so that the distance from the critical density region to the peak density is much shorter. Hence, the mass contained between peak and critical density is greatly reduced and this, to a large extent, compensates for the reduced conductivity.

As a test of the consistency of our two codes, we performed a calculation with the 2D code in a 1D mode. All the quantities were initialized with no y-variation (the y-direction being transverse to the laser beam) and this uniformity persisted throughout the run. The results of this run are displayed in the fifth row of Table B2b.I. The agreement between the first and fifth rows is excellent.

Next, we simulated 2D effects by adding a y-variation to the laser intensity. The intensity was uniform in a region 240 μ wide (approximately the experimental spot diameter) and then fell off exponentially on either side. It was much more difficult to extract the numbers needed for a comparison to experiment in this case, and only the entries for the averaged quantities, the two velocities, have been filled in for the sixth row of Table B2b.I. It was too difficult to accurately locate all of the foil mass and so the summed quantities were not calculated. However, the two velocities are sufficient for our purposes. Note that there is a significant drop in the target velocity, as expected, when 2D effects are included. The fact that there was such a small change in the ablation velocity, again as expected, gives us confidence that we were able to extract these average velocities correctly from our 2D calculation.

All of these results were extracted from the computed results at a time corresponding to about 5.5 nsec after the peak intensity was reached. At that time, the laser intensity was down about a factor of fifty and only minor changes should occur at later times. That this was indeed the case was verified in a 1D run that was extended to 18 nsec beyond the intensity peak (corresponding to a flux reduction of over 35 orders of magnitude).

We have found that the internal consistency between a 1D and a 2D computer model to calculate the ablative acceleration of a thin foil by a relatively long pulse, low intensity laser beam is excellent. A purely 1D calculation can adequately describe the mass burn-off and blow-off velocity, but 2D effects or a variable metric 1D geometry must be included to calculate the target velocity to better than 30% accuracy.

As long as reasonable initial profiles are used and the thermal conduction is within an order of magnitude of the classical value, it appears that conservation of mass, momentum and energy are sufficient to give reasonable agreement with experiment. However, detailed understanding of the microscopic processes at work requires more accurate measurements and modeling as well as more information about the density and temperature of the ablation region.

REFERENCES

1. NRL Laser-Plasma Interaction Group, NRL Memo Report No. 3890 (1978), ed. B.H. Ripin; R. Decoste et al., Phys. Rev. Lett. **42**, 1673 (1979); B.H. Ripin et al., Phys. Rev. Lett. **43**, 350 (1979).

2. O.N. Krokhin et. al., Sov. Phys. JETP **42**, 107 (1976); N.G. Basov et. al., Sov. Phys. JETP Lett. **26**, 433 (1977); J.P. Anthes, M.A. Gusinow, and M. Keith Matzen, Phys. Rev. Lett. **41**, 1300 (1978).

3. J.M. McMahon, NRL Memo Report No. 3591 (1977), ed. S.E. Bodner.

4. R.E. Kidder, Nucl. Fusion **8**, 3 (1968); K.A. Brueckner, P.M. Campbell, and R.A. Grandy, Nucl. Fusion **15**, 471 (1975); S.J. Gitomer, R.L. Morse, and B.S. Newberger, Phys. Fluids **20**, 234 (1977); R.C. McCrory and R.L. Morse, Phys. Rev. Lett. **38**, 544 (1977); F.S. Felber, Phys. Rev. Letter, **39**, 84 (1977); J.D. Perez and G.L. Payne, Phys. Fluids **22**, 361 (1979).

5. J.P. Boris, NRL Memo Report No. 4022 (1979).

6. J.P. Boris, and D.L. Book in "Methods of Computational Physics" **16**, 85 (1976); J.P. Boris in "Comments on Plasma Physics and Controlled Fusion" **3**, 1 (1977); Inertial Confinement Fusion at NRL, S. Bodner, et al., IAEA-CN-37-B-3 Proceedings of the Innsbruck IAEA Conference, 1978.

7. S.I. Braginskii in "Review of Plasma Physics" **1**, 205, ed. M.A. Leontovich.

8. J.H. Orens, NRL Memo Report 4167 (1980).

Table B2b.I
A Comparison of Calculations to Experiment for a 15μ
CH Foil Irradiated with a 10^{13} w/cm^2 Peak Intensity

	$\frac{\Delta M}{M_o}$ (%)	η_h (%)	U (10^7 cm/sec)	V (10^6 cm/sec)
1D Solution A	20	10.4	3.2	7.6
1D Solution A $K_0 = K_0/10$	17	9.0	3.6	6.9
1D Solution B	20	9.9	3.3	7.4
1D Solution B $K_0 = K_0/10$	16	8.7	3.6	6.8
2D Solution A (1D Mode)	21	10.8	3.1	8.0
2D Solution A (3D Mode)	—	—	3.0	6.8
EXPERIMENT[a]	$25^{+\ 8}_{-\ 5}$	$6.6^{+\ 20}_{-\ 1.8}$	$3.3 \pm .7$	$5.1^{+\ 1.0}_{-\ 2.6}$

(a) Ref. 1
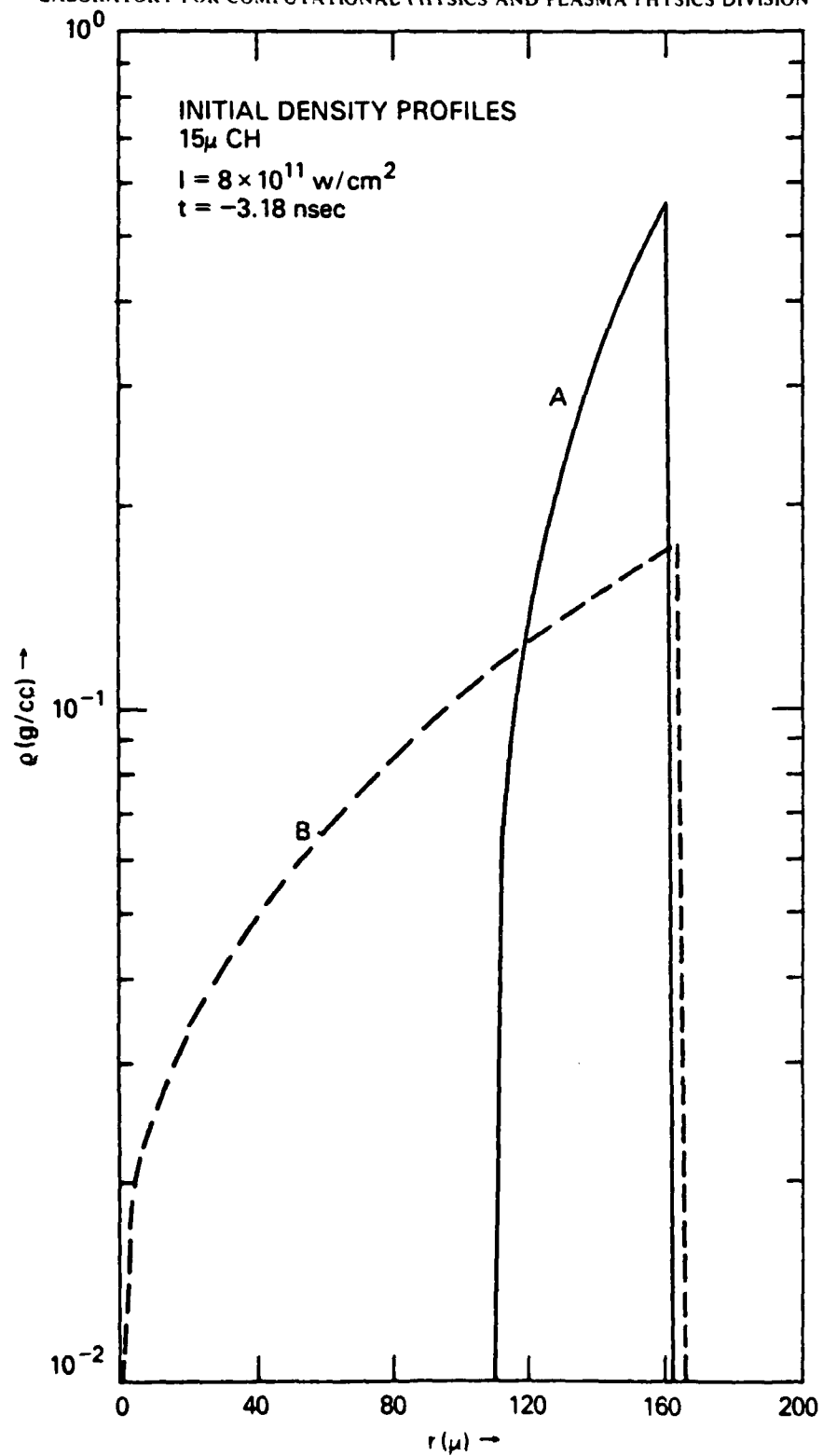
Fig. B2b.1—Two very different initial density profiles corresponding to an absorbed laser intensity of 8×10^{11} w/cm^2 and a 15μ CH target. This is incident from the right.
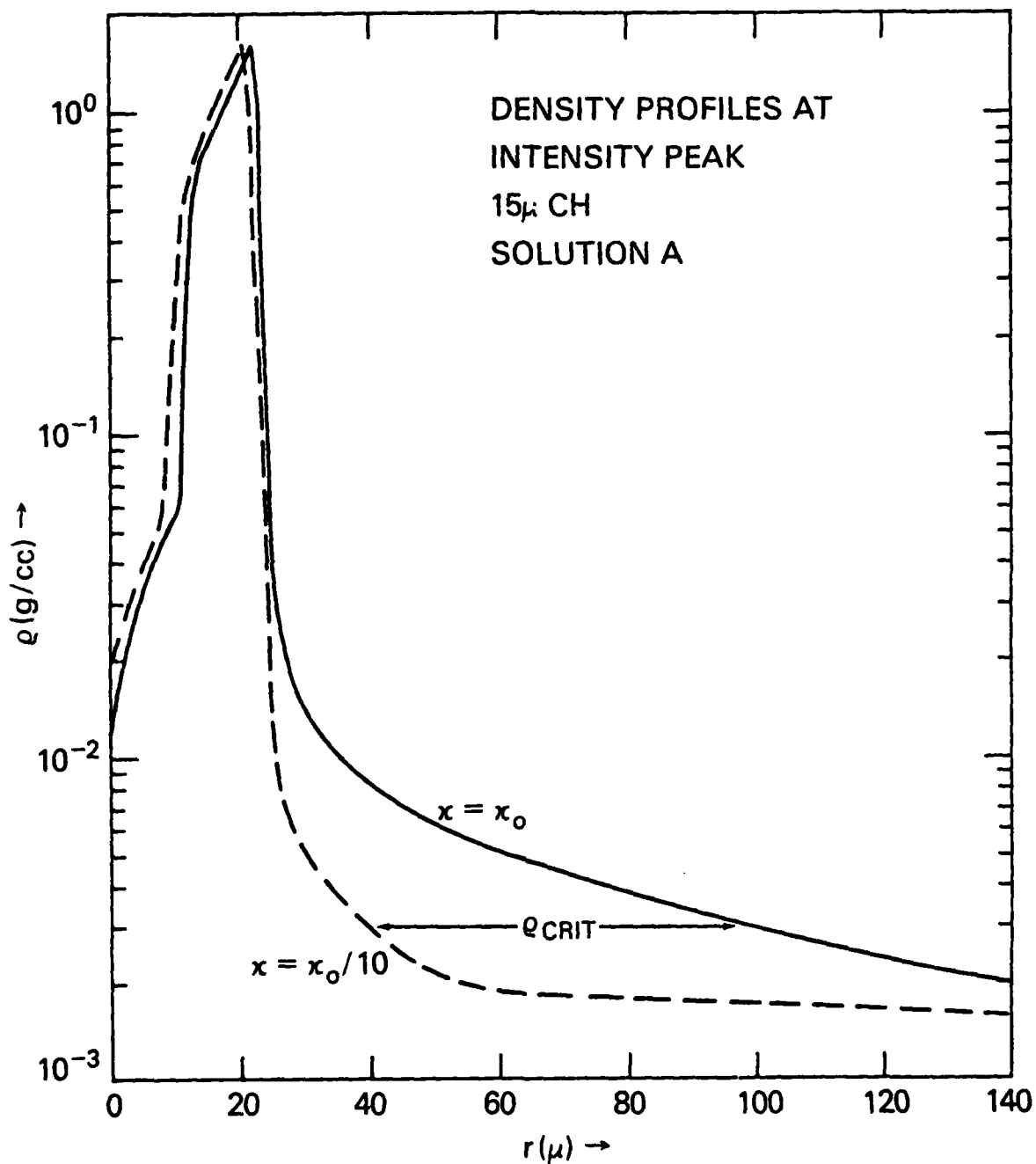
42

Fig. B2b.2—Two density profiles at the time of the peak intensity that both evolved from initial solution A. Only the thermal conduction coefficients differ for the two cases as labelled. Note the large difference in the location of the critical density relative to the density peak. This figure is based on results from our 1D calculations. Again, the laser is incident from the right.

C. DEVELOPMENT OF COMPUTATIONAL TECHNIQUES

Realistic numerical calculations of the Rayleigh-Taylor instability at interior material interfaces require accurate advancement of the material interfaces. This requirement favors the use of a Lagrangian formulation because Eulerian techniques must either employ special procedures to locate an interface or use excessively fine gridding to resolve it. Unfortunately these Eulerian procedures are not only cumbersome and time consuming, but result in a numerical diffusion which can grow large enough to mask the physical motion of the interface. The price that is paid for ease in locating an interface in a Lagrangian treatment is a distorted or skewed grid in all but the simplest of flows.

A badly distorted grid can always be regularized by an Eulerian rezone phase, but only at the expense of reintroducing numerical diffusion. The accuracy of these calculation is then limited to the accuracy of the rezone algorithms, which are often less accurate than the corresponding strictly Eulerian treatments. Since the purpose of rezoning is to maintain a roughly central position for a vertex relative to its neighbors, an alternative solution would be to allow the grid to reconnect as vertices migrate in the flow to reflect their new relative positions. Unfortunately, a single line reconnection on a quadrilateral grid replaces two quadrilateral cells with one triangular and one pentagonal cell, an therefore requires special differencing algorithm in the neighborhood of the reconnection. In general this means that grid reconnections for a quadrilateral mesh must be global and can result in a quadrilateral mesh only for periodic grid anomalies.

In contrast, if a triangular grid is used instead of a quadrilateral mesh, any reconnected grid line must result in two triangles. Grid anomalies can be resolved locally without recourse to global rezoning and cannot result in changing the character of grid zones. Vertices can also be added or deleted where required to maintain resolution with only local grid changes. In other words, it is possible to dynamically alter a triangular grid at a given location with the effects of the alteration being felt only by the vertices near that location. This fact opens up the possibility of conserving physical variables locally even during grid restructuring. In the hydrodynamics code SPLISH this goal is attained through the use of conservation laws expressed as integrals over regions about each vertex and over triangles or pairs of

44

triangles. Grid reconnections, vertex additions or vertex deletions result in the unambigious definition of new cell quantities through the use of these integral invariants. Regridding algorithms can therefore be formulated which are completely automated and local and which preserve conserved physical variables.

The incompressible fluid code SPLISH incorporates these algorithms into a general connectivity hydrodynamics code using a triangular grid. Calculations of the Rayleigh-Taylor instability with SPLISH had previously been extended well into the nonlinear regime. Figure C.1 illustrates one earlier calculation which modeled the effect of the unstable pusher-ablator interface on the stable pusher-fuel interface. The lowest region in the figure represents the ablator which is separated from the pusher by an interface that is given an initial sinusoidal perturbation. The fuel is represented by the ungridded region above the pusher and is separated from it by a free surface. The shape of the interface at four times in the calculation is shown in both the plots of the triangular grid and the pathlines. Pathline plots record the current and five previous positions of each vertex. The development of Kelvin-Helmholtz vortices on the interface due to the progressively strengthening shear is evident in the pathlines.

The addition of gridding algorithms to permit attachment of the heavier fluid at the bottom of the computational region extended these runs considerably. The accelerating columns of dense pusher eventually replaced the ablator along most of the ablation front, leaving a thin column of ablator being pumped toward the fuel by the vortex pair. A complex flow of mixed pusher and ablator continued to alter the vorticity "baroclinically" at each of the vertices and a jet of pusher was shown to impinge into the fuel region. At this point in the calculation higher resolution was desirable as well as an improved treatment of reattachment at the free surface. Therefore the fuel region itself was gridded and runs were begun with better resolution.

Gridding beyond the free surface and within cavities simplifies the grid restructuring problems there but leaves unresolved the question of improved boundary conditions at the free surface. At a free surface pressures are assumed to be given. Although this defines pressure gradients as well, the

boundary condition is not yet sufficiently specified. Pressures are used in the interior of the fluid to maintain a flow consistent with the chosen equation of state ($\nabla \cdot V = 0$ in SPLISH). Therefore, at the surface some other means of satisfying this condition must be found for the partial surface vertex cells.

Currently the code adjusts the free surface positions to keep the surface layer divergence-free. Therefore the free surface boundary in now treated in a manner analogous to that used at rigid boundaries—by vertex movement. Vertices at a rigid boundary are moved to locations enforced by the contour of the boundary. At the free surfaces, movement of the vertices provides for divergence-free flow about the vertex. This boundary condition has now been implemented and has eliminated a previous mode of failure due to the presence of tangential velocities at the free surface. Although this formulation is more consistent and improves the free surface behavior, the free surface motion is still problematic in that a first order approximation is used. Higher order solutions are currently being sought.

Improved resolution for the calculations was also needed, but could be achieved only by recoding. Although the number of vertices could be increased easily by a factor of 4, this is only a doubling of resolution in either direction. The construction of a larger code evolved into three major work areas. First, large outdated portions of old code were cleaned out. This includes the old method of marker particles which had been superceded by the current pathlines as well as the elimination of large amounts of common area which was being used inefficiently. The decrease in core needed for the program increased the total number of vertices that can be used in a practical calculation to roughly 2000, almost 50% more than possible before the clean-up.

As Figure C.2 illustrates, the finer resolution runs permitted much improved detail for several features of the late-time flow. A thin ribbon of pusher remains between the ablator and fuel at this time. The jet formed above the main column of pusher has collapsed, entraining two bubbles of fuel. Similar "bubbles" of pusher within the ablator and ablator within the pusher are found within the vortex pair. The pathlines are of course much shorter in this simulation because of the decreased timestep necessary at this point in the calculation due to the Courant condition.

46

Figures C.3 and C.4 illustrate another calculation in which an initial mode 2 perturbation to the interface contained a slight mode 3 admixture. The gross behavior of the interface is similar to the earlier calculations except that the two "spikes" no longer progress at the same rate. Furthermore, it is evident in the last frame that the higher mode structure has accelerated the growth of secondary vortices near the thinned pusher.

Second, work has been undertaken on improving the elliptic solver. Particularly at large array sizes, the elliptic solver overwhelmingly dominates the cost of a simulation, and a more rapid convergence could make very large array sizes practical. As a first attempt at such an improvement, a totally scalar version was implemented which used SOR and which improved the rate of convergence substantially. However, after several tests this approach was abandoned, since the gains in rate of convergence were offset by the greatly increased computation times. A vectorized version executes much more rapidly on the TI-ASC, so that the vectorized, poorly converging algorithm is far less costly than the scalar, rapidly converging one. Efforts are now underway to find other means of solving the elliptic equations which are more adapted to the particular problems presented by a general triangular mesh.

Although our results indicate that the code is nearly ready for a systematic study of the influence of the Rayleigh-Taylor instability on the ablation dynamics, some code modifications still need to be performed. The analysis of the pressure fields generated in current runs indicates fluctuation due to variations in the velocity fields. These velocity fluctuations have in turn been traced to the rotation operator used in SPLISH to conserve vorticity. Exact conservation of vorticity in a Lagrangian code was attempted for the first time in SPLISH. This exact conservation narrows the choice of rotation operators to a single possible operator. However, this exact operator can induce the pressure fluctuations described above in regions of large shear. Vertices in the shear layer experience an added divergence from the rotation operator. Since this added divergence is numerical and not physical, SPLISH is currently being altered to iteratively reduce these added divergences. Such a solution retains the exact conservation of vorticity yet eliminates any spurious numerical divergence in regions of shear.

While this modification is being implemented, another alteration is also being coded. Velocities are placed at the triangle centroids in SPLISH. During reconnection, a quadrilateral velocity is conserved, as well as vorticity and divergence about all vertices. However, despite this conservation each of the four affected vertices experience a net acceleration due to the weighting procedure used in assigning vertex velocities. A new weighting procedure is being implemented concurrently with the new rotation operator to eliminate these accelerations.

Both of these alterations were found to be necessary primarily through the use of new diagnostic routines for the velocity fields. These routines were formulated to aid in debugging the added gridding routines mentioned previously. A side effect of their use should be improved convergence for our elliptic solver due to the elimination of divergences introduced through both the rotator and velocity weighting. The addition of these divergences to the physical flow-induced divergences implies spurious pressure changes which could be eliminated previously only by more iterations in the solver.

Efforts are also underway to construct a fully single precision version of the code to both decrease the CPU time and storage currently used by SPLISH. Although the bulk of the gridding routines are currently single precision, the main hydrodynamic routines have been double precision. This had mistakenly been thought necessary in the past to ensure convergence of the elliptic solver. Preliminary tests indicate that the new rotation operator eliminates the need for double precision in these routines.

And third, an effort has been initiated to standardize the routines used in this project. A change of array sizes or particular problem generally has meant a change to most subroutines in the code. This led to multiple versions of source code. A perhaps inevitable result of multiple versions has been their gradual evolution and mutation into different codes instead of different versions of the same code, and an accompanying rise in errors due to this multiplicity. Standardization will eliminate this source of error.

Several presentations have been given on the results of the Lagrangian calculations. These include the following oral papers:

"Simulations of the Nonlinear Development of the Rayleigh-Taylor Instability for Inertial Confinement Fusion" at the Boston APS meeting, 1979.

"Occurrence of the Rayleigh-Taylor Instability in Inertial Confinement Fusion" at the Fluid Dynamics sectional APS meeting at Notre Dame, 1979.

and

"Some Considerations of Rayleigh-Taylor Instability in Inertial Confinement Fusion" at the 1980 CLEOS/ICF meeting.

In addition, the calculations discussed here are featured in a chapter on the triangular grid technique in a forthcoming book, *Recent Developments in Computational Techniques for Applied Hydrodynamics*, Springer-Verlag.
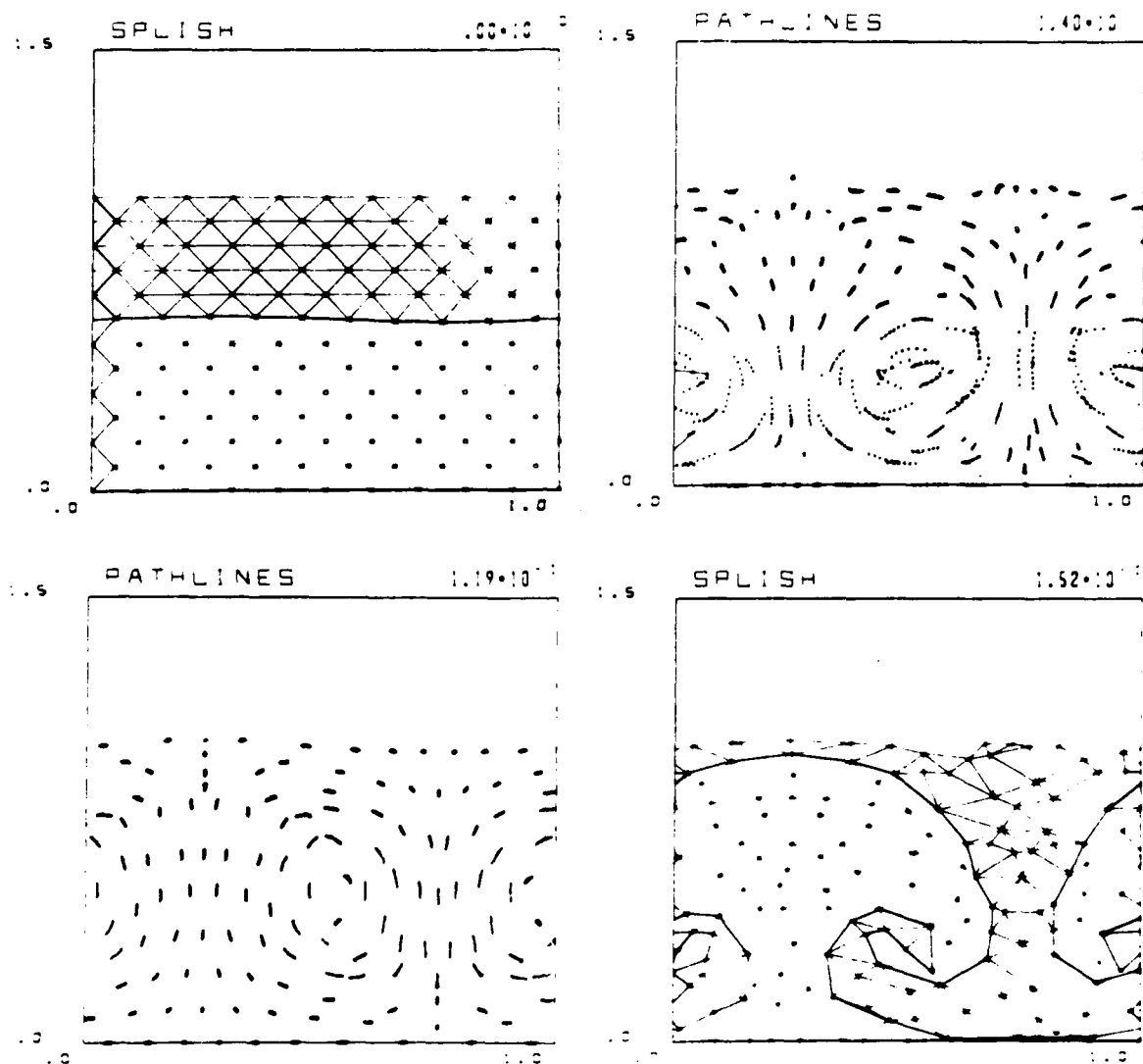
Fig. C.1 — Flow patterns, interface location and grid structure of the internal interface Rayleigh-Taylor instability as computed by the SPLISH computer code. The upper left quadrant of the figure shows the initial grid of triangles with a small sinusoidal perturbation of the interface at $t = 0$. The initial velocities (in the accelerating frame of reference) were all taken to be zero. The lower left quadrant shows the flow field as the instability enters its nonlinear phase. The vertex locations are plotted at successive timesteps to give streaks whose length is proportional to the local fluid velocity. Shear flow is established as the interface steepens, giving rise to vortices centered on the interface in a flow which has been likened to the onset of the Kelvin-Helmholtz instability. In the two right-hand quadrants, two fluids are beginning to mix in the Rayleigh-Taylor vortices and the rate of fall of the heavy material is no longer increasing.
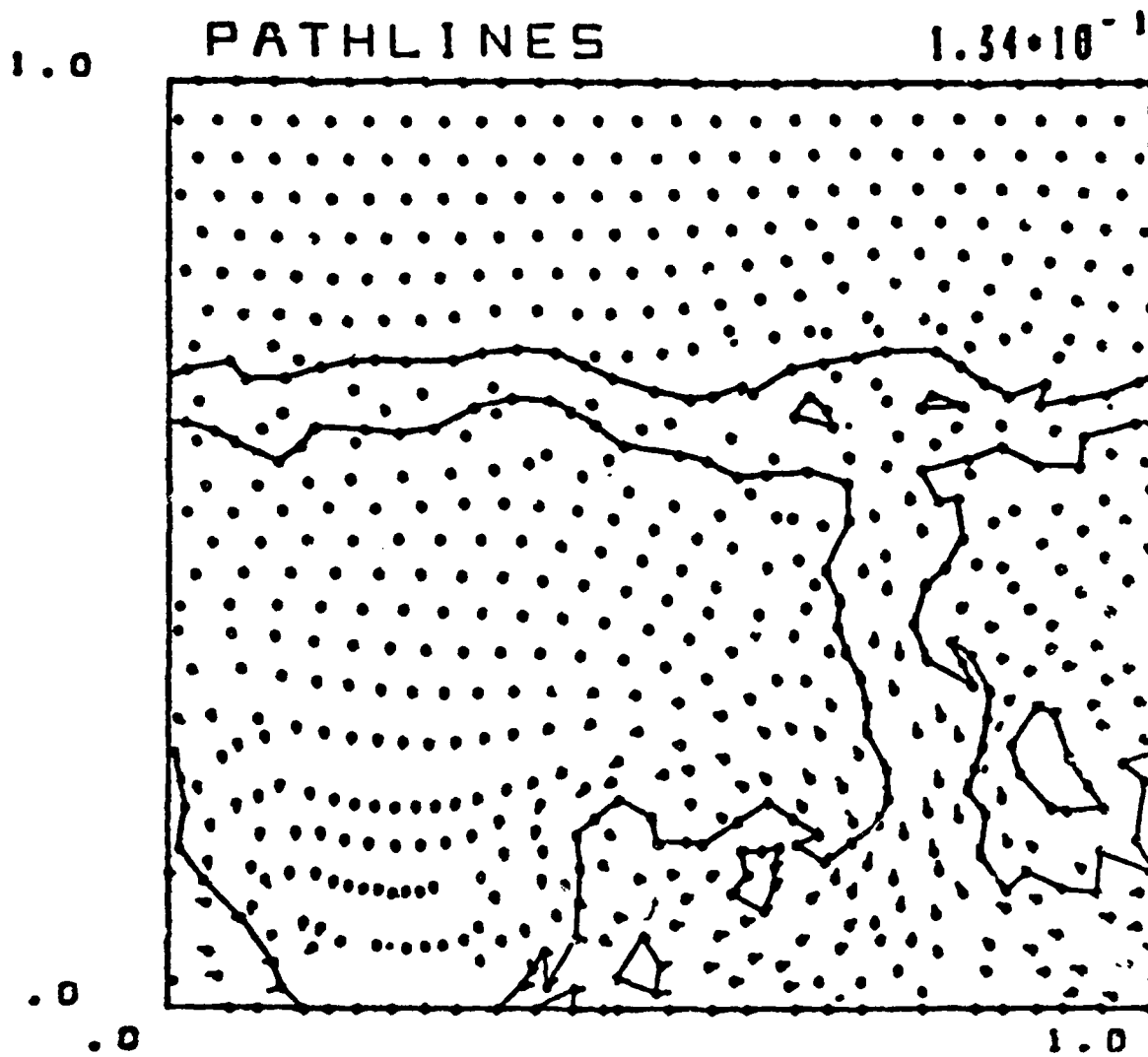
Fig. C.2 — The Rayleigh-Taylor instability at a later time using finer resolution. Evidence of smaller scale structure includes secondary vortices, collapsing jets, waves on the ribbon of pusher, and entrained "bubbles" of fuel, ablator, and pusher.
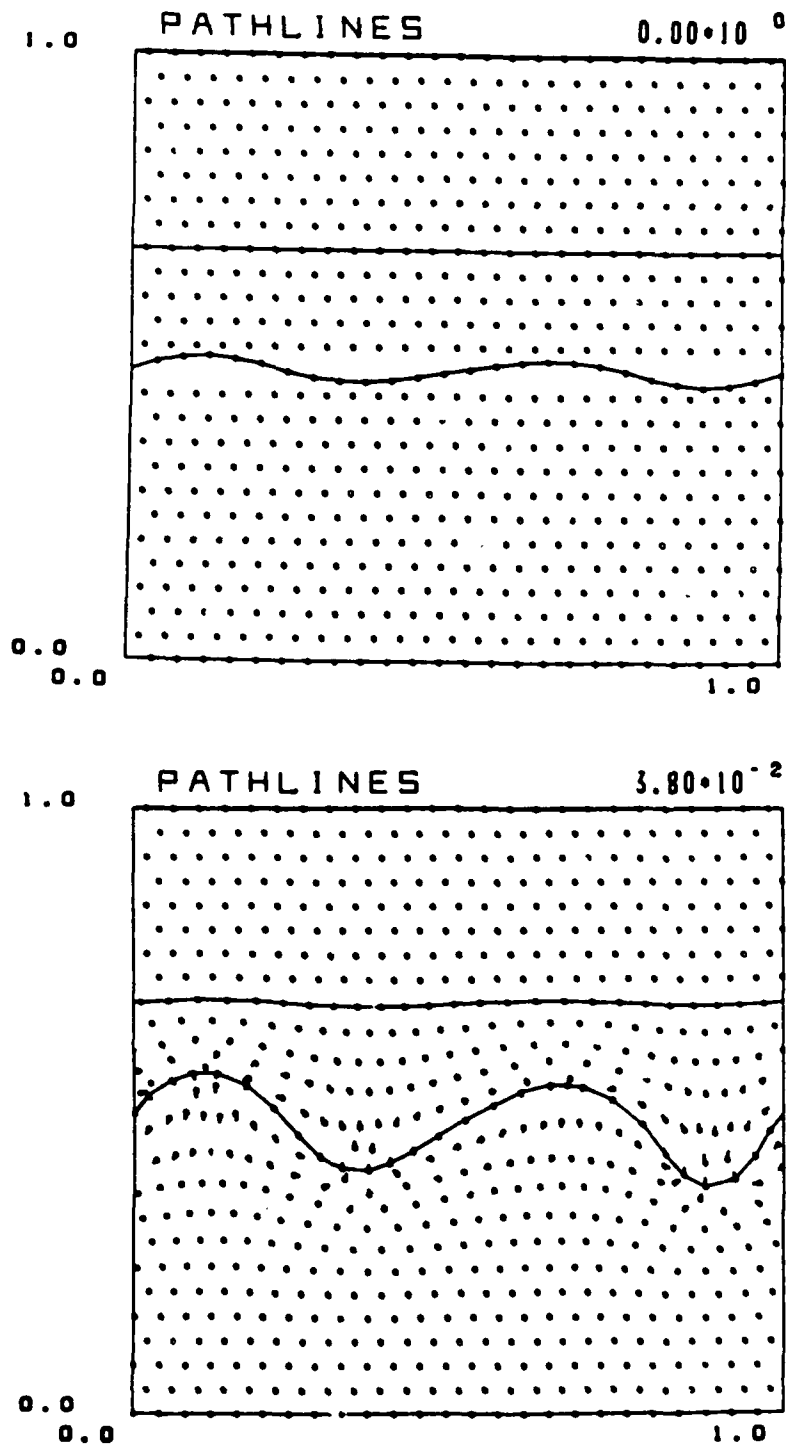
Fig. C.3 — The initial development of the Rayleigh-Taylor instability with a dominant mode 2 perturbation. An admixture of mode 3 is evident in the asymmetry in both the X and Y directions.
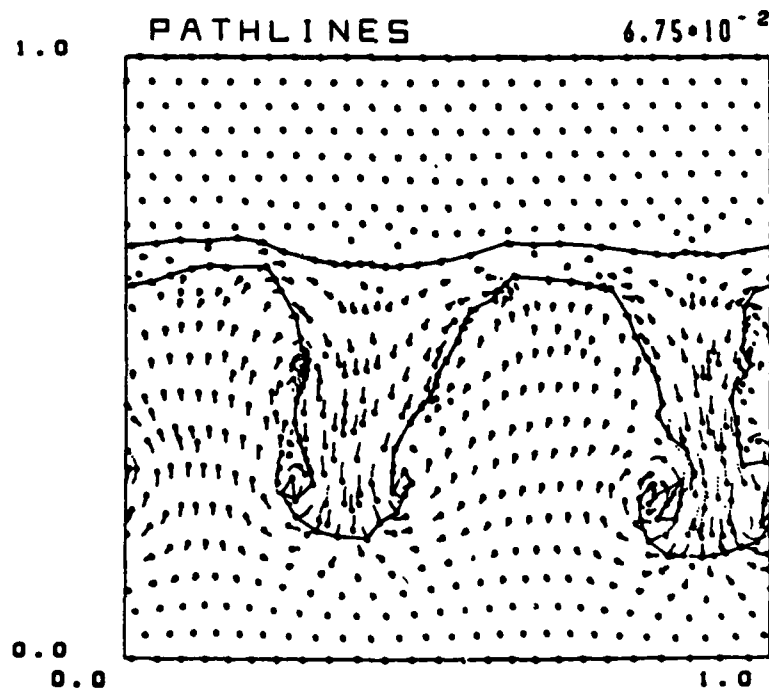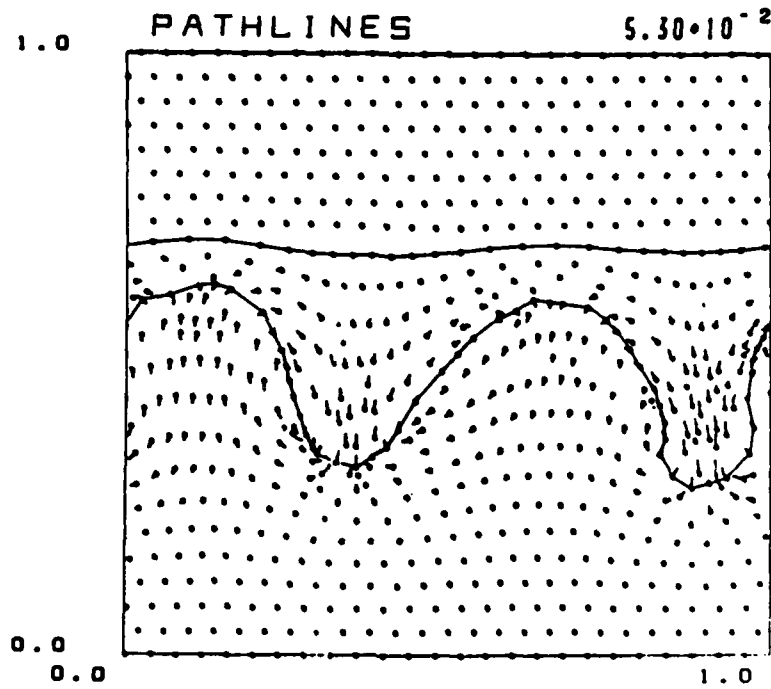
PATHLINES $5.30 \cdot 10^{-2}$

Fig. C.4 — Nonlinear development of the mixed mode 2 and mode 3 calculation of Fig. C.3. The mode 3 admixture has led to different levels of entrainment for each spike, but the vertical descent is roughly similar.

53

D1. Discussion of the Quasi-Static Equilibrium Parameter Space

In our earlier work[1]; we developed analytic approximations and numerical solutions for the structure of quasi-static laser driven ablation layers. At that time we discussed the dependence of the structure on two independent dimensionless parameters M_0 and N_0. M_0 is the isothermal mach number at the density peak, which for our situation is usually a small number, and N_0 is the Péclet number at the density peak (thermal diffusion time scale/free streaming time scale), which in our regime is usually a large number. Since thermal diffusion and free streaming are dominant mechanisms in our ablation model it is reasonable they should parameterize the solution. Although M_0 and N_0 are the most convenient parameters for the analysis it will be shown subsequently that the acceleration and entropy of the shell can equally well parameterize the solution.

Within certain limitations, the choice of values for M_0 and N_0 is arbitrary. In essence, there is not a unique equilibrium for the prescribed physical constraints, laser intensity, and shell mass, but various accessible equilibria. Exactly which equilibria would occur for a given physical situation might be determined by the necessarily time-dependent evolution leading up to that equilibrium. Two such effects might be the entropy and acceleration of the shell imparted by an initial shock. Recently we analyzed the $M_0 - N_0$ parameter space for curves of constant shell entropy and acceleration. The results of such an analysis for 15 μ C-H and an intensity of 10^{13} w/cm^2 are given in Fig. D1.1. The curves of constant entropy are nearly straight lines with slopes approximately inversely proportional to the magnitude of the entropy. Initially, visual inspection seemed to imply that all the straight lines emanated from a point on the negative M_0 axis, but more detailed analysis seems to show that the curves are not straight near $M_0 = 0$ and begin to bend toward the origin. Further analysis will be necessary before the exact intersection point can be determined. The curves of constant acceleration are somewhat like hyperbolas, with the curves for increasing acceleration being further from the origin. Note that only a small variation in the acceleration causes large variations in M_0 and N_0. In our earlier work we identified two regions for the pressure profile. Below the curve $N_0 M_0^2 = .4\sqrt{3}$ (shown as the lower dashed curve on Fig. D1.1) the pressure profile cannot have a turning point and the pressure

increases monotonically out to the critical surface. This would correspond to a case where the density and pressure gradients are always opposite in sign from the density maximum until the critical surface. Such a case would be expected to be Rayleigh-Taylor unstable. Above this curve the pressure profile can turn over and yield a region where the density and pressure gradients are again of like sign. Recent investigation has shown that there is a transition region between the case where the pressure only increases and where it reaches a maximum and then decreases out to the critical surface. Previously we have shown that

$$\text{sign}\left[\frac{dP}{d\zeta}\right] = \text{sign}\left[\frac{2}{M_0^2} - \frac{d\eta}{d\zeta}\right].$$

Therefore in the former case $\frac{d\eta}{d\zeta}$ never gets as large as $\frac{2}{M_0^2}$ while in the latter case once it does become larger it never becomes smaller again before reaching the critical surface. Recent numerical analysis has observed the transition between the two cases where $\frac{d\eta}{d\zeta}$ does again become smaller than $\frac{2}{M_0^2}$ prior to the critical surface and the pressure profile again increases. This region is enclosed between the two dashed curves on Fig. D1.1. As the equilibrium moves from the lower dashed curve to the upper one, the second turning point moves closer to the critical surface. Therefore by moving from the lower to the upper dashed curve the overall region where the density and pressure gradients are opposite in sign becomes smaller. Above the upper dashed curve there is only a very small region of opposed gradients and this is the profile considered in most previous analyses. It is interesting to note that the shape of these dashed curves very much resembles the curves for constant acceleration. Therefore the results seem to imply that below a certain acceleration the pressure never turns over while above a certain acceleration there is only one turning point for the pressure. Of course, further study is required before making a firm statement. Outside the largest constant acceleration curve on Fig. D1.1, the flow out of the critical surface is no longer supersonic. This region is excluded from the analysis since subsonic flow in the underdense gas would require the temperature to increase away from the heat source at x_c which would be unphysical.[2] Again the onset of this region seems to be strongly dependent on the acceleration.

Since the determination of a specific equilibrium depends on the entropy and acceleration of the foil which are not, in general, specifiable quantities we also investigated the possible existence of evolutionary trends for the various types of "quasi-static" pressure profiles. Using idealized fully time-dependent calculations at constant laser intensity we have noted that profiles in which the pressure turns over seem to retain their basic form, while profiles in which the pressure continually increases seem to evolve into profiles in which the pressure turns over. We conjecture that the latter solution evolves such that the entropy of the foil remains constant while the acceleration of the foil increases into a region where the pressure would then turn over. Figure D1.2a shows the temporal evolution of a "quasi-static" equilibrium with a continually increasing pressure profile, while Fig. D1.2b shows the relative invariance of a "quasi-static" equilibrium with a pressure profile that turns over. These evolutionary trends are very interesting since they seem to imply that the only physically realizable equilibria might be those in which the pressure profile has a turning point and hence is most stable to the Rayleigh-Taylor modes.
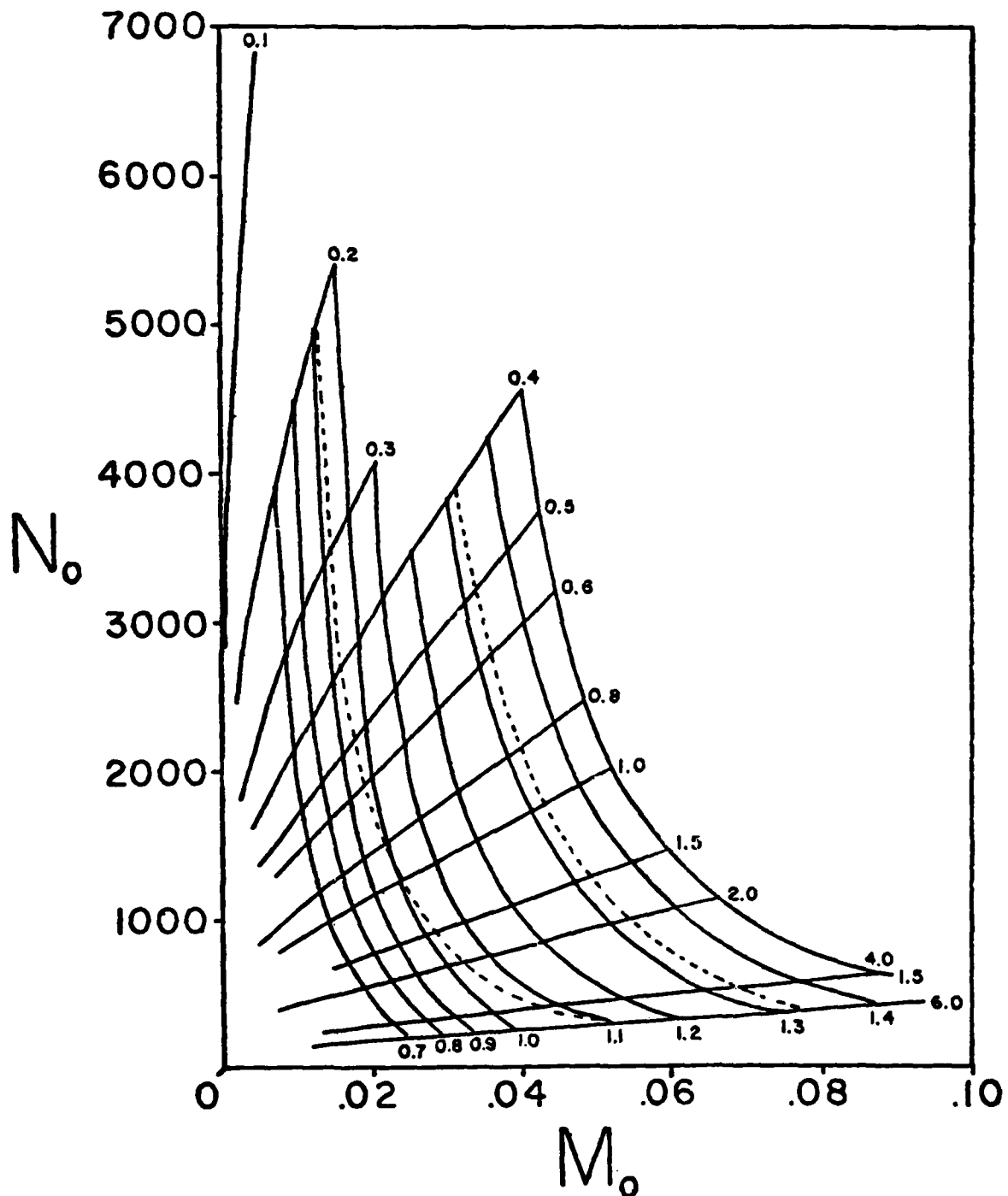
Fig. D1.1 — Contours for constant entropy (nearly straight lines) and constant acceleration (curved lines) in $M_0 - N_0$ space for the case of a 15μ plastic foil irradiated with 10^{13} w/cm^2 laser intensity (80% absorption). Entropy contours are labeled in units of 10^{13} and acceleration contours are labeled in units of 10^{15} cm/sec^2. Dashed lines approximately delineate the regions of stable and unstable cases.
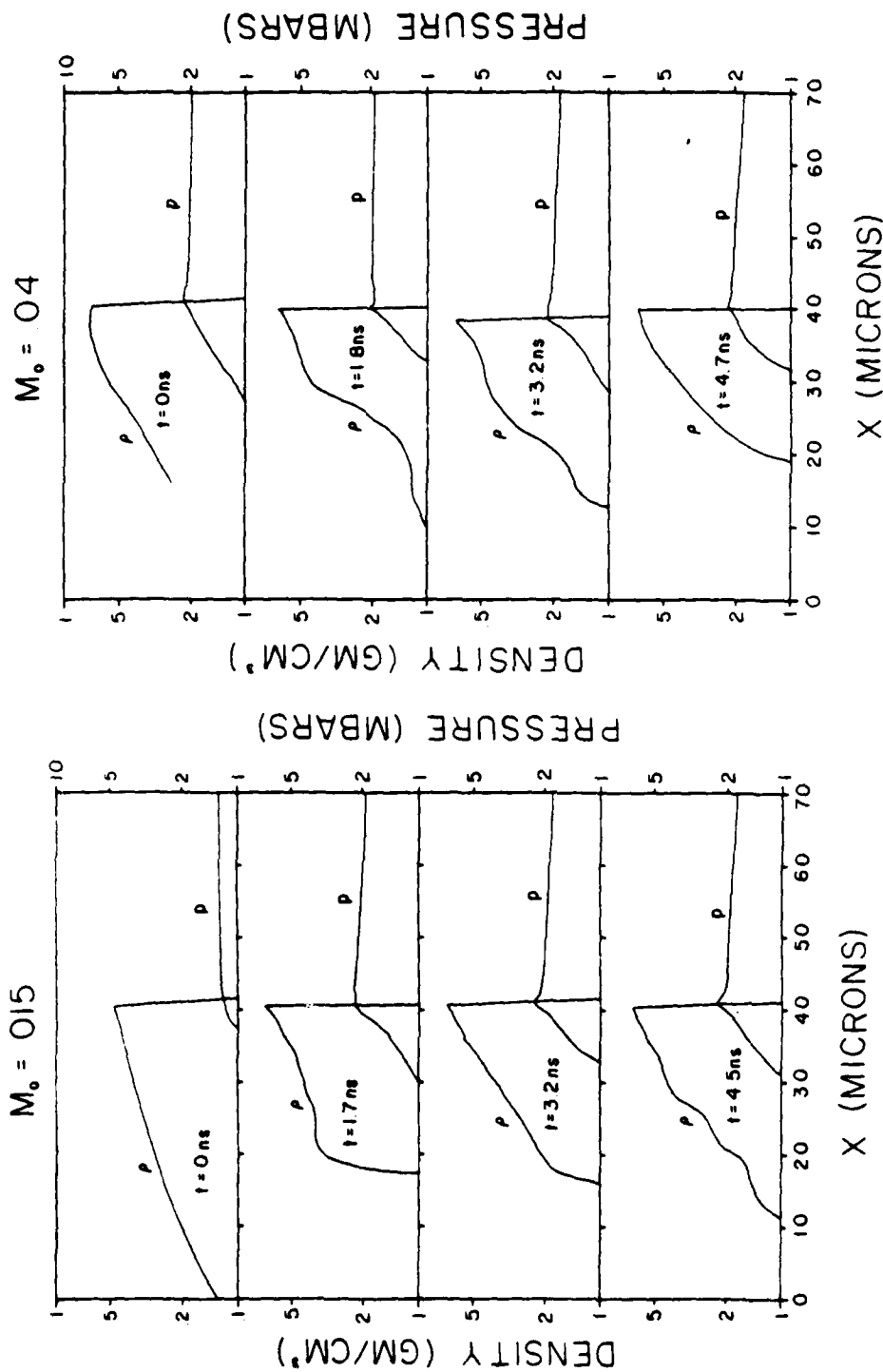
Fig. D1.2—Temporal evolution of two types of "quasi-static" equilibria with the same shell entropy.

D2. The Vorticity Generation Model

One of the most important areas in inertial confinement laser fusion research concerns the Rayleigh-Taylor stability of the ablation layer for laser driven foils and spherical implosions. Since the density and pressure gradients are opposite in sign for that region, simple analysis predicts that perturbations should grow exponentially there. Therefore it is of great interest to determine under what circumstances the expected instability can be stabilized. Our earlier research into the quasi-static (time independent) ablation layer profiles has identified two distinct types of pressure profiles. In the first case the pressure has the intuitively expected turning point and yields a very narrow region where the density and pressure gradients are opposite in sign. In the second case the pressure does not turn over and continues to increase out to the critical surface. Here the region where the density and pressure gradients are opposite in sign is quite broad. There also is a transition region where the pressure does have a local maximum near the density peak, but then at a point between there and the critical surface the pressure increases again. Recently we have utilized a vorticity generation formulation to study the stability of these cases and preliminary results show that the first case is stable while the second is unstable. Complex interactions among the various external parameters determine whether or not the pressure profile turns over, but the predominant indicator is the maximum magnitude of the slope in the ablation region of the dimensionless density profile.

In the usual analysis the vorticity equation is formed by taking the curl of the momentum equation to obtain

$$\frac{\partial \xi}{\partial t} + \nabla \cdot (V\xi) - \xi \cdot \nabla V = \frac{\nabla \rho \times \nabla P}{\rho^2} \tag{1}$$

where $\xi \equiv \nabla \times V$ is the vorticity, ρ is the density, P is the pressure, and the source term on the right hand side is the baroclinic vorticity generation term. In two dimensions, here treated as cartesian, ξ reduces to a single scalar component which will be taken along the z axis. Thus the third term on the left hand side of Eq. (1) vanishes and the equation reduces to:

$$\frac{\partial \xi}{\partial t} + \nabla \cdot (\mathbf{V}\xi) = \frac{\nabla \rho \times \nabla P}{\rho^2} \tag{2}$$

where $\xi_z(x, y, t) \equiv (\nabla \times V)_z = \frac{\partial v}{\partial x} - \frac{\partial u}{\partial y}$, and u and v are respectively velocities in the $\hat{x}$ and $\hat{y}$ direc-

tions. Linearizing Eq. (2) with respect to an equilibruim flow only in the $\hat{x}$ direction and independent

of y and z yields for the first order perturbation (tilde) quantities

$$\rho \frac{\partial}{\partial t} \left[\frac{\partial \tilde{v}}{\partial x} - \frac{\partial \tilde{u}}{\partial y} \right] + \rho \frac{\partial}{\partial x} \left[u \left(\frac{\partial \tilde{v}}{\partial x} - \frac{\partial \tilde{u}}{\partial y} \right) \right] = \frac{1}{\rho} \left(\frac{\partial \rho}{\partial x} \frac{\partial \tilde{P}}{\partial y} - \frac{\partial \tilde{\rho}}{\partial y} \frac{\partial P}{\partial x} \right). \tag{3}$$

Since for the equilibrium

$$\frac{\partial \rho}{\partial t} + u \frac{\partial \rho}{\partial x} + \rho \frac{\partial u}{\partial x} = 0 \tag{4}$$

Eq. (3) may be written

$$\frac{\partial}{\partial t} \left[\rho \left(\frac{\partial \tilde{v}}{\partial x} - \frac{\partial \tilde{u}}{\partial y} \right) + \frac{\partial}{\partial x} \left[\rho u \left(\frac{\partial \tilde{v}}{\partial x} - \frac{\partial \tilde{u}}{\partial y} \right) \right] \right] + \rho \left(\frac{\partial \tilde{v}}{\partial x} - \frac{\partial \tilde{u}}{\partial y} \right) \frac{\partial u}{\partial x} = \frac{1}{\rho} \left(\frac{\partial \rho}{\partial x} \frac{\partial \tilde{P}}{\partial y} - \frac{\partial \tilde{\rho}}{\partial y} \frac{\partial P}{\partial x} \right). \tag{5}$$

After some manipulation and using the first order y momentum equation

$$\frac{\partial \tilde{v}}{\partial t} + u \frac{\partial \tilde{v}}{\partial x} = - \frac{1}{\rho} \frac{\partial \tilde{P}}{\partial y} \tag{6}$$

Eq. (7) becomes

$$\frac{\partial}{\partial t} \left[\frac{\partial}{\partial x} (\rho \tilde{v}) - \frac{\partial}{\partial y} (\rho \tilde{u}) \right] + \frac{\partial}{\partial x} \left\{ u \left[\frac{\partial}{\partial x} (\rho \tilde{v}) - \frac{\partial}{\partial y} (\rho \tilde{u}) \right] \right\} + \left[\frac{\partial}{\partial x} \left(\rho \tilde{v} \frac{\partial u}{\partial x} \right) - \frac{\partial}{\partial y} \left(\rho \tilde{u} \frac{\partial u}{\partial x} \right) \right]$$

$$= - \frac{1}{\rho} \frac{\partial \tilde{\rho}}{\partial y} \frac{\partial P}{\partial x}. \tag{7}$$

It is interesting to note that the pressure perturbation does not appear in Eq. (7).

In studies of Rayleigh-Taylor stability it is usually sufficient to consider incompressible perturba-

tions. Furth, Killeen and Rosenbluth[3] and Coppi, Green and Johnson[4] used this approach for plasma

slab stability and Kidder justified it for isentropic implosions.[5] Thus the first order velocity can be

derived from the curl of a vector potential.

$$\tilde{u} \equiv \frac{\partial \tilde{\psi}}{\partial y} \quad \text{and} \quad \tilde{v} \equiv - \frac{\partial \tilde{\psi}}{\partial x}. \tag{8}$$

Letting

$$\tilde{\zeta} \equiv \frac{\partial}{\partial x} (\rho \tilde{v}) - \frac{\partial}{\partial y} (\rho \tilde{u}) \tag{9}$$

yields a potential equation of the form

$$\frac{\partial}{\partial x}\left[\rho\,\frac{\partial\tilde{\psi}}{\partial x}\right] + \frac{\partial}{\partial y}\left[\rho\,\frac{\partial\tilde{\psi}}{\partial y}\right] = -\tilde{\zeta}. \tag{10}$$

Differentiating the first order continuity equation

$$\frac{\partial\tilde{\rho}}{\partial t} + \frac{\partial}{\partial x}\,(u\tilde{\rho}) = -\tilde{u}\frac{\partial\rho}{\partial x} = -\frac{\partial\tilde{\psi}}{\partial y}\,\frac{\partial\rho}{\partial x} \tag{11}$$

with respect to y yields

$$\frac{\partial\tilde{\chi}}{\partial t} + \frac{\partial}{\partial x}\,(u\tilde{\chi}) = -\frac{\partial^2\tilde{\psi}}{\partial y^2}\,\frac{\partial\rho}{\partial x} \tag{12}$$

where
$$\tilde{\chi} \equiv \frac{\partial\tilde{\rho}}{\partial y}.$$

In this representation Eq. (7) becomes

$$\frac{\partial\tilde{\zeta}}{\partial t} + \frac{\partial}{\partial x}\,(u\tilde{\zeta}) = -\frac{1}{\rho}\,\frac{\partial P}{\partial x}\,\tilde{\chi} + \frac{\partial}{\partial x}\left[\rho\,\frac{\partial u}{\partial x}\,\frac{\partial\tilde{\psi}}{\partial x}\right] + \frac{\partial}{\partial y}\left[\rho\,\frac{\partial u}{\partial x}\,\frac{\partial\tilde{\psi}}{\partial y}\right]. \tag{13}$$

Considering perturbations of the form

$$\tilde{f} = \tilde{f}\,(x,\,t)\,\exp\,(iky). \tag{14}$$

Eqs. (10), (12), and (13) become

$$\frac{\partial}{\partial x}\left[\rho\,\frac{\partial\tilde{\psi}}{\partial x}\right] - k^2\rho\tilde{\psi} = -\tilde{\zeta} \tag{15a}$$

$$\frac{\partial\tilde{\chi}}{\partial t} + \frac{\partial}{\partial x}\,(u\tilde{\chi}) = k^2\,\frac{\partial\rho}{\partial x}\,\tilde{\psi} \tag{15b}$$

$$\frac{\partial\tilde{\zeta}}{\partial t} + \frac{\partial}{\partial x}\,(u\tilde{\zeta}) = -\frac{1}{\rho}\,\frac{\partial P}{\partial x}\,\tilde{\chi} + \frac{\partial}{\partial x}\left[\rho\,\frac{\partial u}{\partial x}\,\frac{\partial\tilde{\psi}}{\partial x}\right] - k^2\rho\,\frac{\partial u}{\partial x}\,\tilde{\psi}. \tag{15c}$$

Equations (15a), (15b), and (15c) become the basis for the vorticity generation model. Nowhere in the analysis have the zero order quantities been assumed to be independent of time so these equations can just as well be applied to study the stability of time dependent situations. If the condition of an incompressible perturbation is relaxed then Eq. (15a) would take the form of a wave equation allowing the presence of sound waves to govern the onset of motion at one point after vorticity is generated at another.

D2a. Vorticity Generation Model Tests and Application to Laser Driven Ablation Profiles

Prior to applying our vorticity generation model to the actual laser ablation profiles we tested the method in cases of an accelerating step density discontinuity where the answers are known analytically. Figure D2a.1 shows the density profile for the cases chosen. Equilibria both with and without mass flow were considered. In the cases without mass flow the growth rate of the Rayleigh-Taylor modes is given by the standard formula

$$\gamma = \sqrt{kgA} \tag{16a}$$

where

$$A \equiv \frac{\rho_a - \rho_b}{\rho_a + \rho_b}. \tag{16b}$$

Previous authors[6,7] have considered the cases with constant mass flow and approximate theoretical analysis yields for the growth rate.

$$\gamma^2 + 2k \, \frac{u_a}{u_b} \, (u_b - u_a)\gamma - kgA \approx 0 \tag{17a}$$

In the limit where $\frac{\rho_a}{\rho_b} \gg 1$ and $\frac{g}{ku_a^2} \gg 1$ this reduces to

$$\gamma \approx \sqrt{kg} - ku_a \tag{17b}$$

which is identical to the results of Bodner.[7]

In order to test the vorticity generating code, the case shown in Fig. D2a.1 was run with $\rho u = 0$. In Fig. D2a.2, the analytical dispersion relation Eq. (16a) is plotted as the solid line and our numerical results as solid circles. As can be seen, the agreement is excellent over a wide range of wavelengths. In order to get this agreement, it was found that very fine resolution ($\Delta x \approx 10^{-6}$ cm) i· the unstable region was needed at the shortest wavelength. This was accomplished by utilizing a variably-spaced grid with the finest resolution in the unstable region and with the coarsest resolution at the boundaries.

Also shown in Fig. D2a.2 are the results for $\rho u = 10^5$ cm^{-2} sec^{-1}. The dashed curve is a plot of Eq. (17a) and the open circles are our numerical results. Agreement is reasonable except at the shortest wavelengths where timestep limitations would not allow good enough resolution.

Satisfied that our code was running correctly, we next attempted to analyze the stability of the different kinds of ablation layer profiles that were discussed previously. This was done for a 15μ C-H foil irradiated with a 1×10^{13} w/cm^2 beam and having an 80% absorption rate. We chose two profiles of Fig. D1.2 corresponding to an entropy of 4×10^{12}. The first profile has a monotonically rising pressure profile and hence a broad Rayleigh-Taylor unstable region ($\sim 100\mu$). The other pressure profile peaks just beyond the density peak and decreases from there to the critical surface. Hence, it has a very narrow unstable region ($\sim .03\mu$). The vorticity amplitudes for the first case are shown in Fig. D2a.3 and for the second case in Fig. D2a.4. Whereas the first case show exponential growth, the second case is stable.
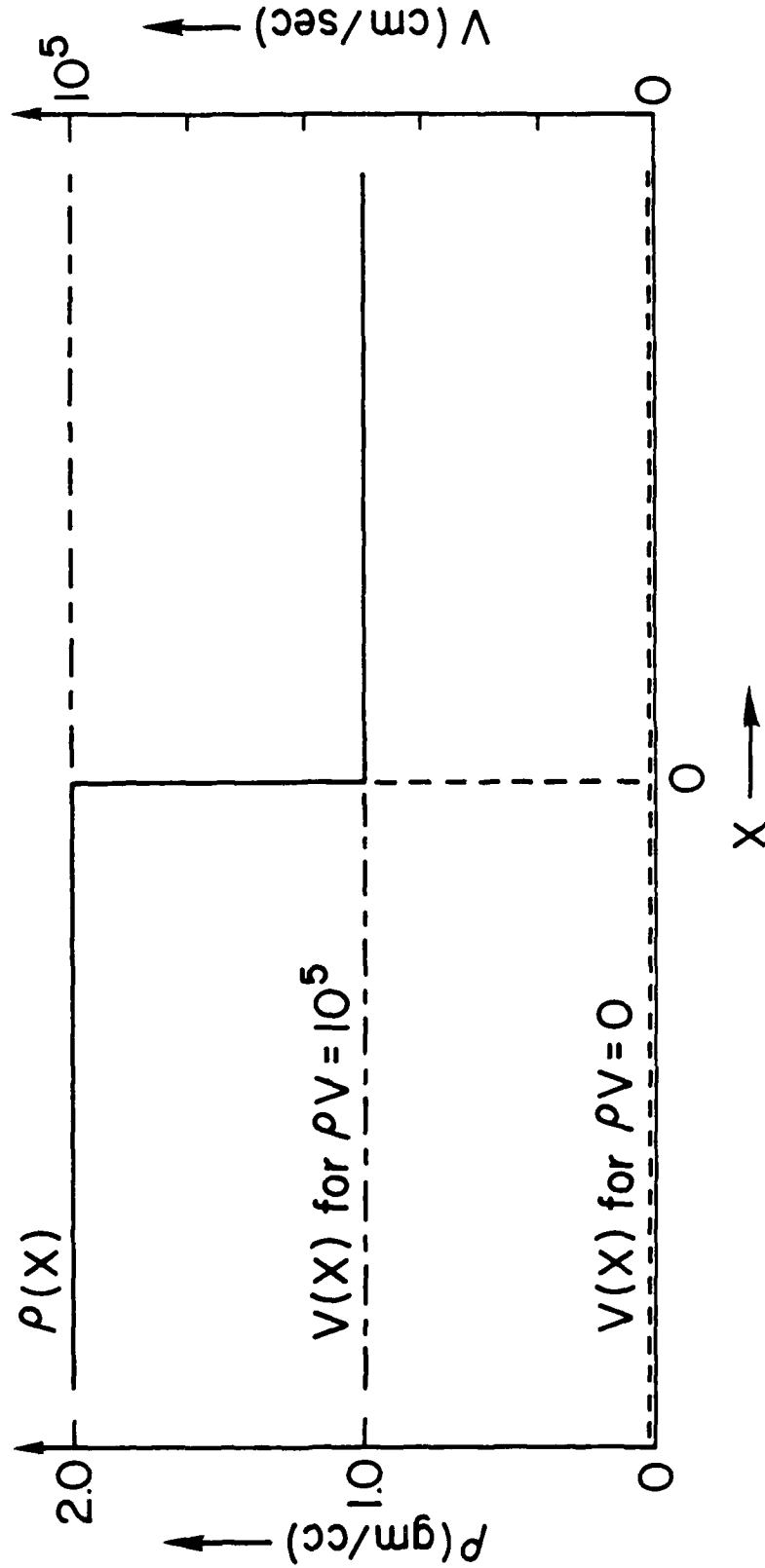
Rayleigh - Taylor Test Profiles

Fig. D2a.1 — Density and velocity profiles for the classical Rayleigh-Taylor case
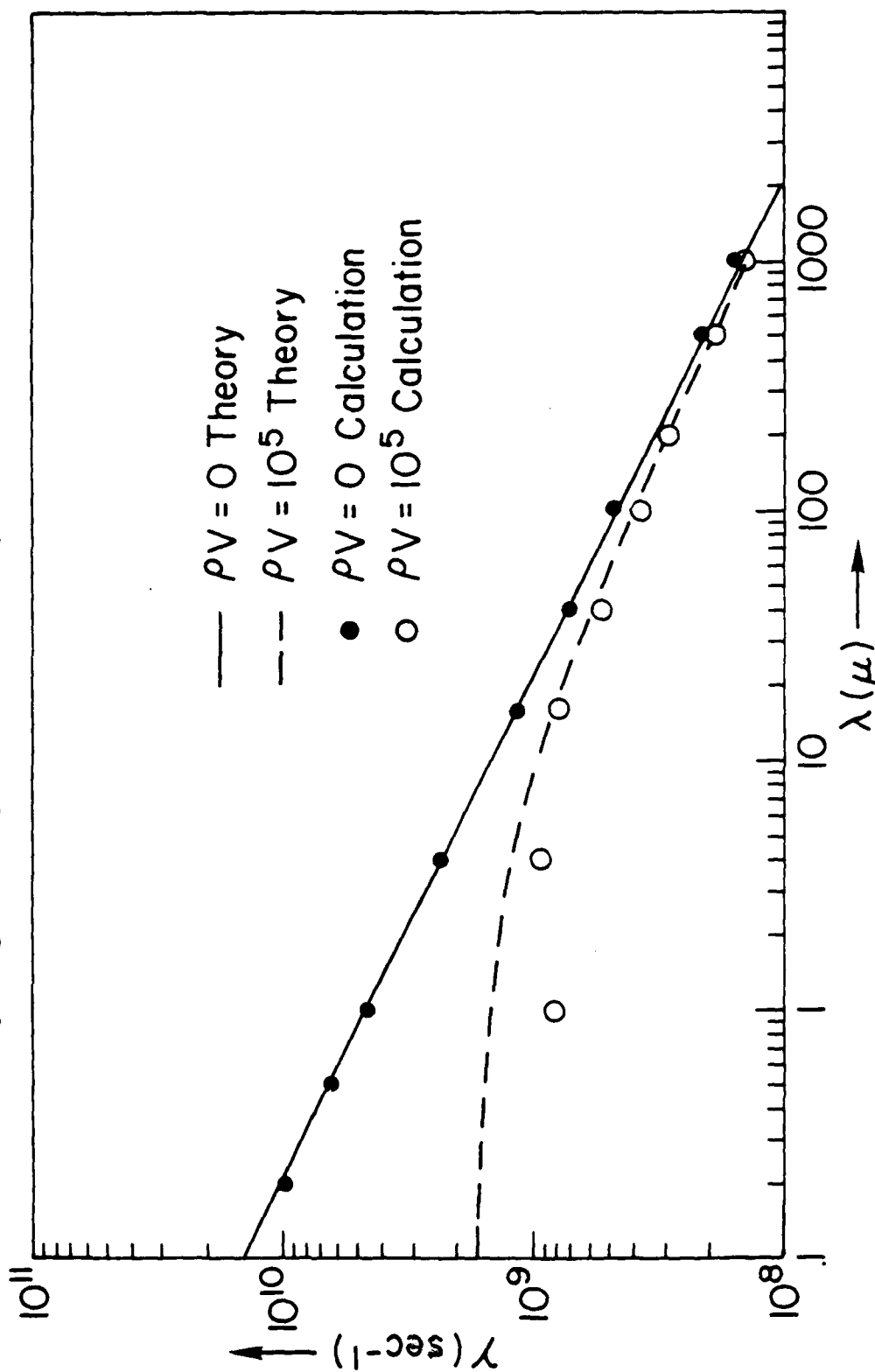
Rayleigh-Taylor Test Dispersion Relations

Fig. D2a.2—Comparison of calculations to the theoretical Rayleigh-Taylor dispersion relations of equations (1a) (solid line) and (2a) (dashed line) for the profiles of Fig. D2a.1.
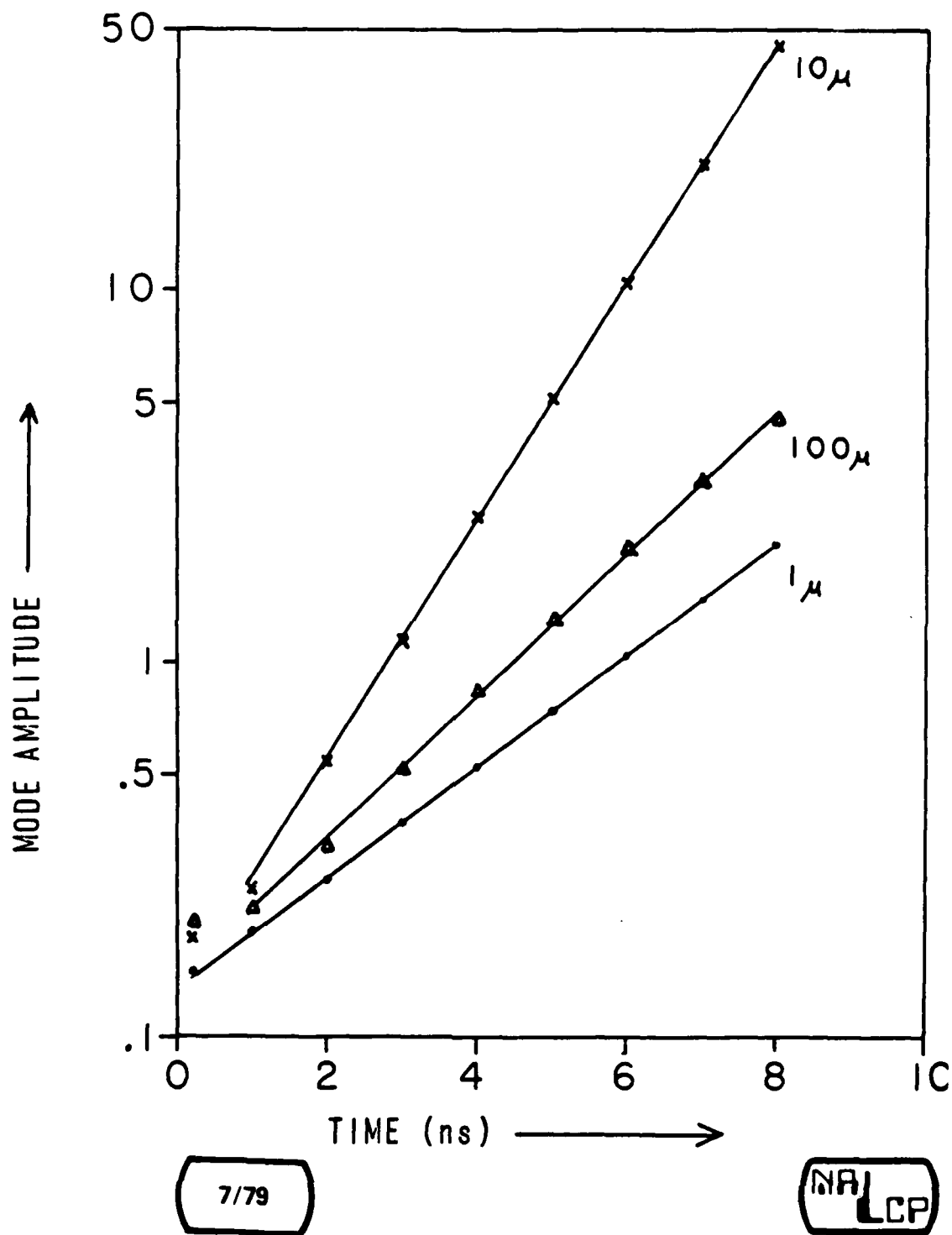
Fig. D2a.3—Mode amplitudes for 15μ plastic foil irradiated with 10^{13} w/cm^2 laser intensity. These amplitudes are for the unstable case where $M_0 = .015$, $N_0 = 2610$, and $S_0 = 4 \times 10^{12}$.
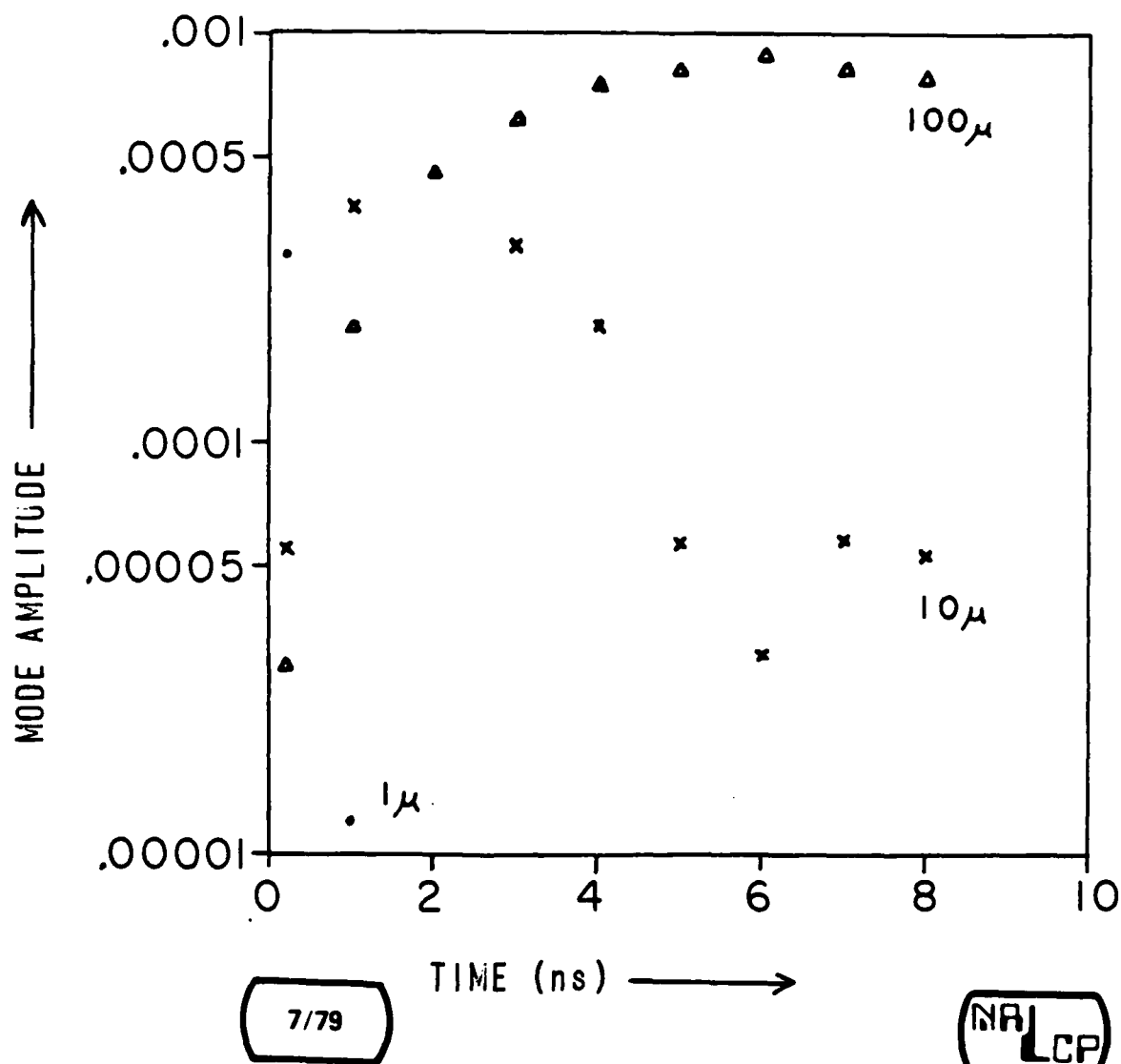
CASE #2   R-T STABLE

Fig. D2a.4—Mode amplitudes for the same external parameters as Fig. D2a.3 but in the stable region where $M_0 = .04$, $N_0 = 4560$, and $S_0 = 4 \times 10^{12}$.

D3. Development of an Eigenvalue Equation

Equations (15a), (15b), and (15c) of the vorticity generation model can be utilized as the basis for the development of an eigenvalue equation to analytically investigate the stability of a time independent zero order state. Assuming that the perturbations $\tilde{f}$ go as

$$\tilde{f}(x,t) = \tilde{f}(x) \exp{(\gamma t)} \tag{18}$$

Eqs. (15a), (15b), and (15c) become

$$\frac{d}{dx}\left[\rho \, \frac{d\tilde{\psi}}{dx}\right] - k^2\rho\tilde{\psi} = -\tilde{\zeta} \tag{19a}$$

$$\gamma\tilde{\chi} + \frac{d}{dx}(u\tilde{\chi}) = k^2\frac{d\rho}{dx}\tilde{\psi} \tag{19b}$$

and

$$\gamma\tilde{\zeta} + \frac{d}{dx}(u\tilde{\zeta}) = -\frac{1}{\rho}\frac{dP}{dx}\tilde{\chi} + \frac{d}{dx}\left[\rho\frac{du}{dx}\frac{d\tilde{\psi}}{dx}\right] - k^2\rho\frac{du}{dx}\tilde{\psi}. \tag{19c}$$

Equations (19b) and (19c) are greatly simplified for a zero order state with no velocity.

$$\frac{d}{dx}\left[\rho \, \frac{d\tilde{\psi}}{dx}\right] - k^2\rho\tilde{\psi} = -\tilde{\zeta} \tag{20a}$$

$$\gamma\tilde{\chi} = k^2 \frac{d\rho}{dx}\tilde{\psi} \tag{20b}$$

$$\gamma\tilde{\zeta} = -\frac{1}{\rho}\frac{dP}{dx}\tilde{\chi} \tag{20c}$$

Combining Eqs. (20a), (20b), and (20c) into a single eigenvalue equation yields

$$\frac{d}{dx}\left[\rho\frac{d\tilde{\psi}}{dx}\right] - k^2\rho\tilde{\psi} = \frac{k^2}{\gamma^2}\frac{1}{\rho}\frac{dP}{dx}\frac{d\rho}{dx}\tilde{\psi} \tag{21}$$

where Eq. (21) is of the classical Sturmian type and since it is self-adjoint allows a variational formulation

$$\frac{\gamma^2}{k^2} = -\frac{\int \frac{1}{\rho}\frac{dP}{dx}\frac{d\rho}{dx}|\tilde{\psi}|^2 \, dx}{\int \rho\left[\left|\frac{d\tilde{\psi}}{dx}\right|^2 + k^2|\tilde{\psi}|^2\right] dx}. \tag{22}$$

From Eq. (22) it is clear that a system with opposed pressure and density profiles can be unstable. For a step density discontinuity the eigenfunction is of the form $\exp{(-k|x|)}$ and Eq. (22) reduces to the familiar form of Eq. (16a) where

$$\frac{1}{\rho} \frac{dP}{dx} = g. \tag{23}$$

For the case of a time independent zero order state with finite mass flow Eqs. (19a), (19b), and (19c) can be somewhat simplified by use of the zero order continuity and momentum equations

$$\frac{d}{dx}(\rho u) = 0 \text{ or } \rho u = \text{constant} \tag{24}$$

and

$$\frac{d}{dx}(P + \rho u^2) = \rho g \text{ or } \frac{1}{\rho} \frac{dP}{dx} = g - u \frac{du}{dx} \tag{25}$$

By subtracting u times Eq. (19b) from (19c) and substituting for the gradient of pressure, Eq. (19c) may be written as

$$\gamma \left[\bar{\zeta} - u\bar{\chi} + \frac{d\rho}{dx} \frac{d\bar{\psi}}{dx} \right] + \frac{d}{dx} \left[u \left(\hat{\zeta} - u\bar{\chi} + \frac{d\rho}{dx} \frac{d\bar{\psi}}{dx} \right) \right] = -g\bar{\chi} + \gamma \frac{d\rho}{dx} \frac{d\bar{\psi}}{dx} \tag{26}$$

Defining

$$\bar{\zeta}' = \bar{\zeta} - u\bar{\chi} + \frac{d\rho}{dx} \frac{d\bar{\psi}}{dx} \tag{27}$$

and dropping the primes Eqs. (19) become

$$\rho \frac{d^2\bar{\psi}}{dx^2} - k^2\rho\bar{\psi} = -\bar{\zeta} - u\bar{\chi} \tag{28a}$$

$$\gamma\bar{\chi} + \frac{d}{dx}(u\bar{\chi}) = k^2 \frac{d\rho}{dx} \bar{\psi} \tag{28b}$$

$$\gamma\bar{\zeta} + \frac{d}{dx}(u\bar{\zeta}) = -g\bar{\chi} + \gamma \frac{d\rho}{dx} \frac{d\bar{\psi}}{dx}. \tag{28c}$$

Defining

$$\bar{\zeta}' = u\bar{\zeta} \exp\left[\int \frac{\gamma}{u} dx \right] \tag{29}$$

and dropping the primes Eqs. (28) can be transformed into two coupled second order differential eigenvalue equations.

$$\frac{d}{dx} \left[\rho u \exp\left(-\frac{\gamma u}{g} \right) \frac{d\bar{\psi}}{dx} \right] - k^2\rho u \exp\left(-\frac{\gamma u}{g} \right) \bar{\psi} = -\exp\left(-\int \frac{\gamma}{u} dx - \frac{\gamma u}{g} \right) \left[\bar{\zeta} - \frac{u^2}{g} \frac{d\bar{\zeta}}{dx} \right] \tag{30a}$$

$$\frac{d}{dx} \left[u\frac{d\bar{\zeta}}{dx} \right] = -gk^2 \frac{d\rho}{dx} \exp\left[\int \frac{\gamma}{u}dx \right] \bar{\psi} + \frac{d}{dx} \left[\gamma u\frac{d\rho}{dx} \exp\left[\int \frac{\gamma}{u} dx \right] \frac{d\bar{\psi}}{dx} \right]. \tag{30b}$$

And from Eqs. (24) and (25)

$$\int \frac{\gamma}{u} \, dx = \gamma \frac{P + \rho u^2}{\rho \, ug} \tag{31}$$

Equations (30) can then be solved numerically for a given zero-order state.

REFERENCES

1. J.H. Orens, NRL Memo Report 4167 (1980).

2. F.S. Felber, "Steady-State Model of a Flat Laser-Driven Target," Phys. Rev. Lett. **39**, 84 (1977)

3. H.P. Furth, J. Killeen, and M.N. Rosenbluth, "Finite-Resistivity Instabilities of Sheet Pinch," Phys. Fluids, **6**, 459 (1963).

4. B. Coppi, J.M. Greene, and J.L. Johnson, "Resistive Instabilities in a Diffuse Linear Pinch," Nucl. Fusion **6**, 101 (1966).

5. R.E. Kidder, "Laser-Driven Compression of Hollow Shells: Power Requirements and Stability Limitations," Nucl. Fusion **16**, 3 (1976).

6. L. Baker, "Stability of Ablation and Combustion Fronts," Phys. Fluids **21**, 295 (1978).

7. S.E. Bodner, "Rayleigh-Taylor Instability and Laser-Pellet Fusion," Phys. Rev. Lett. **33**, 761 (1974).

PLANS FOR THE EXTENSION AND CONTINUATION OF OUR RESEARCH IN INERTIAL CONFINEMENT FUSION

We plan to cntinue our research in three areas. The first is a continued development of the Lagrangian triangular grid techniques including compressible flow modifications and diffusive transport. These generalizations are logical extensions of our previous development work in the geometry control and re-configuration techniques of the triangular grid algorithms. Along with this we plan to investigate non-local techniques for solving certain general types of elliptic problems because the nature of our tri-angular grid techniques tends to defeat most of the known fast solution algorithms for this class of problems. The second area is to complete our analysis of the stability of shock collapse and compare our analytic solutions with our computational model based on the Chester, Chisnell, and Whitham approximation. We also plan to extend our closed form solution for the linear stability of the "Guderley"-like imploding shock into the nonlinear regime through use of the numerical model. Finally, the third area is to continue the development and application of our vorticity generation model (VGM) to the problem of Rayleigh-Taylor stability in the laser-driven ablation layer. We plan to relax the incompressibility constraint on the perturbation and examine the effects of finite sound speed. We also plan to use the VGM to help resolve many of the ambiguities in previous Rayleigh-Taylor stability investigations due to the inability to properly include convection in the analytic analyses and the inabil-ity to allow high enough resolution in the numerical studies.